Induced polarization signatures of cations exhibiting differential sorption behaviors in saturated sands

Pierre Vaudelet, André Revil, Myriam Schmutz, Michel Franceschi, P. Bégassat

Induced polarization signatures of cations exhibiting differential sorption behaviors in saturated sands

P. Vaudelet,[1] A. Revil,[2,3] M. Schmutz,[1] M. Franceschi,[1] and P. Bégassat[4]

[1] Two sets of experiments were designed to understand the change in induced polarization associated with the sorption of copper and sodium, exhibiting distinct sorption behavior on a silica sand. A sand column experiment was first performed to see the change in the complex conductivity during the advective transport of a copper sulfate solution. A second set of experiments was done with the sand at equilibrium with various solutions of NaCl and $CuSO_4$. In the first experiment, the copper sulfate solution replaced a sodium chloride solution, keeping the electrical conductivity of the solution nearly constant. During the passage of the copper sulfate solution, the apparent phase angle decreased from 3 ± 0.2 to 0.5 ± 0.2 mrad, while the magnitude of the conductivity of the sand remained nearly constant. A quantitative model is proposed to explain the change in the complex conductivity as a function of the chemistry assuming a polarization mechanism associated with the Stern layer (the inner part of the electrical double layer coating the water-mineral interface). The Stern layer polarization is combined with a complexation model describing the competitive sorption of copper and sodium at the pore water interface. The change of the phase lag is directly associated with the ion exchange between sodium and copper at the surface of the silica grains. The explanation of the observed phase differences between Na and Cu relies on their different complexation behaviors, with Na being loosely absorbed, while Cu forms relatively strong complexation with both inner (monodentate) and outer sphere (bidentate) complexes. The replacement of Cu^{2+} by Na^+ is less favorable; therefore, the kinetics of such a replacement is much slower than for the opposite replacement (Na^+ by Cu^{2+}). We were able to reproduce the changes in the phase lags at thermodynamic equilibrium near the relaxation frequency and in the frequency domain. These measurements and modeling results open the door to the quantitative interpretation of spectral induced polarization data in the field in terms of quantification of the sorption processes.

1. Introduction

[2] Spectral induced polarization is a nonintrusive geophysical method that is able to image the distribution of the magnitude of the complex conductivity (or complex resistivity) and the phase angle between the current and the voltage of porous materials [*Olhoeft*, 1985; *Vanhala*, 1997; *Morgan et al.*, 1999; *Slater and Lesmes*, 2002a]. The magnitude of the resistivity and the phase lag can be written as a complex conductivity or a complex resistivity. These measurements are usually performed in a broad frequency range (typically, 1 mHz to 100 Hz in the field). At higher frequencies, the response of the rock is dominated by electromagnetic coupling and the Maxwell-Wagner polarization [*Olhoeft*, 1985, 1986]. Because spectral induced polarization can be connected to the electrochemistry of the pore water–mineral interface [*Olhoeft*, 1985], this method has been proposed to detect and image contaminant plumes such as oil spills [*Olhoeft*, 1986; *Vanhala*, 1997; *Morgan et al.*, 1999], benzene and ethylene dibromide plumes [*Sogade et al.*, 2006], and organic-matter-rich contaminant plumes associated with leakages from landfills [*Aristodemou and Thomas-Betts*, 2000]. However, the work performed to date in geophysical applications has been rather qualitative. Typically, the response observed in the laboratory or in the field has been fitted by an empirical relationship named the Cole-Cole model (or similar models such as the Cole-Davidson and the generalized Cole-Cole models). Mechanistic models of spectral induced polarization started to emerge 20 years ago in geophysics to predict the electrical behavior of porous materials below 10 kHz [*de Lima and Sharma*, 1992; *Lesmes and Morgan*, 2001]. However, these models were mainly developed to connect spectral induced polarization spectra to textural properties such as permeability [*Slater and Lesmes*, 2002b; *Binley*

[1]Institut EGID, University of Bordeaux 3, Pessac, France.
[2]Department of Geophysics, Colorado School of Mines, Golden, Colorado, USA.
[3]LGIT, UMR 5559, CNRS, University of Savoie, Equipe Volcan, Le Bourget-du-Lac, France.
[4]ADEME, Anger, France.

et al., 2005]. Until recently, these models were not connected to a full description of the electrical double-layer theory or, more importantly, to a speciation model between the components of the pore water and the mineral surface. Therefore, it was not possible to model quantitatively the impact of a change in the pore water chemistry upon the parameters describing spectral induced polarization.

[3] Recently, Revil and colleagues [*Leroy et al.*, 2008; *Leroy and Revil*, 2009; *Jougnot et al.*, 2010; *Revil and Florsch*, 2010; *Schmutz et al.*, 2010] have developed a fundamental theory connecting spectral induced polarization to the speciation of the mineral surface of silicates and aluminosilicates. Their theory is based on a description of the electrochemistry of the mineral surface and its connection with a Stern layer polarization model of the grains. This electrochemical approach was initially developed to model the electrokinetic properties of porous rocks with the goal to better understand self-potential measurements in the field [*Revil et al.*, 1999a, 1999b] and transport properties of clay-rich materials [*Leroy et al.*, 2007; *Jougnot et al.*, 2009]. However, this approach can be used to assess the sensitivity of the spectral induced polarization method to changes in the speciation chemistry of the mineral surface (investigating both the kinetics of sorption and thermodynamic equilibrium), a task that has not been performed to date to the best of our knowledge.

[4] This work therefore represents a preliminary step in developing a detailed mechanistic understanding of the response of spectral induced polarization to monitor preferential sorption mechanisms at the surface of minerals. In this paper, spectral induced polarization is used to monitor the advection of copper sulfate in a porous material. We use a clean silica sand in our experiments because the speciation model at the surface of pure silica is well established [see *Wang and Revil*, 2010, and references therein]. However, we point out that the principles are general and comprehensive enough to be applied to this range of surfaces and electrolyte compositions. The generalization of this approach to the multicomponent electrolyte would allow using the spectral induced polarization method in the field and in the laboratory as a nonintrusive spectral method to provide constraints regarding the kinetics and thermodynamics of sorption reactions and to visualize where, in a contaminant plume, some specific sorption reactions may take place. Obviously, induced polarization alone could never be used to look for all the contaminants and chemical reactions occurring in a contaminated aquifer. However, we feel that the coupling between such a geophysical method and reactive transport codes such as TOUGH-REACT [*Mukhopadhyay et al.*, 2009] or PHREEQC [*Parkhurst and Appelo*, 1999] may be a useful tool in hydrogeophysics to characterize contaminant plumes or to follow amendments in bioremediation.

2. Theoretical Background
2.1. Macroscopic Conductivity Model

[5] We consider a pack of sand grains with the median of the grain size distribution denoted by d_0, assuming a very narrow grain size distribution (the theory described here has recently been generalized to a granular material with an arbitrary grain size distribution by *Revil and Florsch* [2010] and in Appendix A). This mean particle size represents half of the number of particles made up of particles either larger or smaller than this size. We note that $\omega = 2\pi f$ is the angular frequency and f is the frequency of the excitation current or the excitation electrical field. The resulting electrical field or electrical current exhibits a phase lag φ with respect to the electrical current or the electrical field. At low frequency, induced polarization is caused by the existence of the electrical double layer at the surface of the grains [*Dukhin and Shilov*, 2002; *Lyklema*, 2002]. This electrical double layer comprises the Stern layer of sorbed counterions and the diffuse layer (Figure 1a).

[6] If an alternating electrical field **E** is imposed, this field is responsible for three polarization mechanisms, as broadly discussed in the literature, especially in colloidal chemistry [see *Dukhin and Shilov*, 2002; *Lyklema*, 2002, and references therein].

[7] 1. The first polarization mechanism corresponds to the fast displacement of the electrical diffuse layer in the case where there is no overlap in the diffuse layer between different grains (which is so only in the dilute suspension of grains in a background electrolyte). This effect can be seen in Figure 1b, where the diffuse layer is displaced in the direction of the electrical field with respect to the equilibrium situation. This mechanism is similar to the Debye-Falkenhagen effect, which affects the ionic atmosphere of an ion in an electrical field. However, this polarization occurs at frequencies much higher than the low-frequency range used in the present investigation. This effect is likely strongly attenuated in porous materials with contiguity between the grains because of the overlap of the electrical diffuse layer.

[8] 2. The second polarization mechanism occurs in the Stern layer. If mobile, the cations of the Stern layer move in the direction of the electrical field and accumulate on one side of the particle. Because they are not allowed to leave the Stern layer (the sorption-desorption process is too slow with respect to the characteristic time scale of the pulsation of the electrical field), they diffuse back in their surface concentration gradient as long as the frequency is low. The diffusion coefficient of this polarization process is the molecular diffusion coefficient of the counterions in the Stern layer (discussed in Appendix B). At high frequencies, the counterions have no time to build concentration gradients. This mechanism was fully developed by *Schwarz* [1962] and later by *Schurr* [1964] and *de Lima and Sharma* [1992]. However, to avoid confusion, it is worth mentioning that *Schwarz* [1962] was interested in modeling the polarization of the diffuse layer, not the Stern layer. It has been recognized that these assumptions were not valid to model the polarization of the diffuse layer [*Dukhin and Shilov*, 2002]. The characteristic frequency separating low and high frequencies depends on the distribution of polarization length scales. These polarization length scales are related to the grain size distribution plus the heterogeneities associated with the roughness of the pore water−grain interface as demonstrated by *Leroy et al.* [2008]. This will be discussed further in section 5.

[9] 3. The third polarization mechanism is associated with the diffuse layer and is called the membrane polarization in geophysics. It corresponds to an increase of the salt concentration to the right side of the grain and a depletion
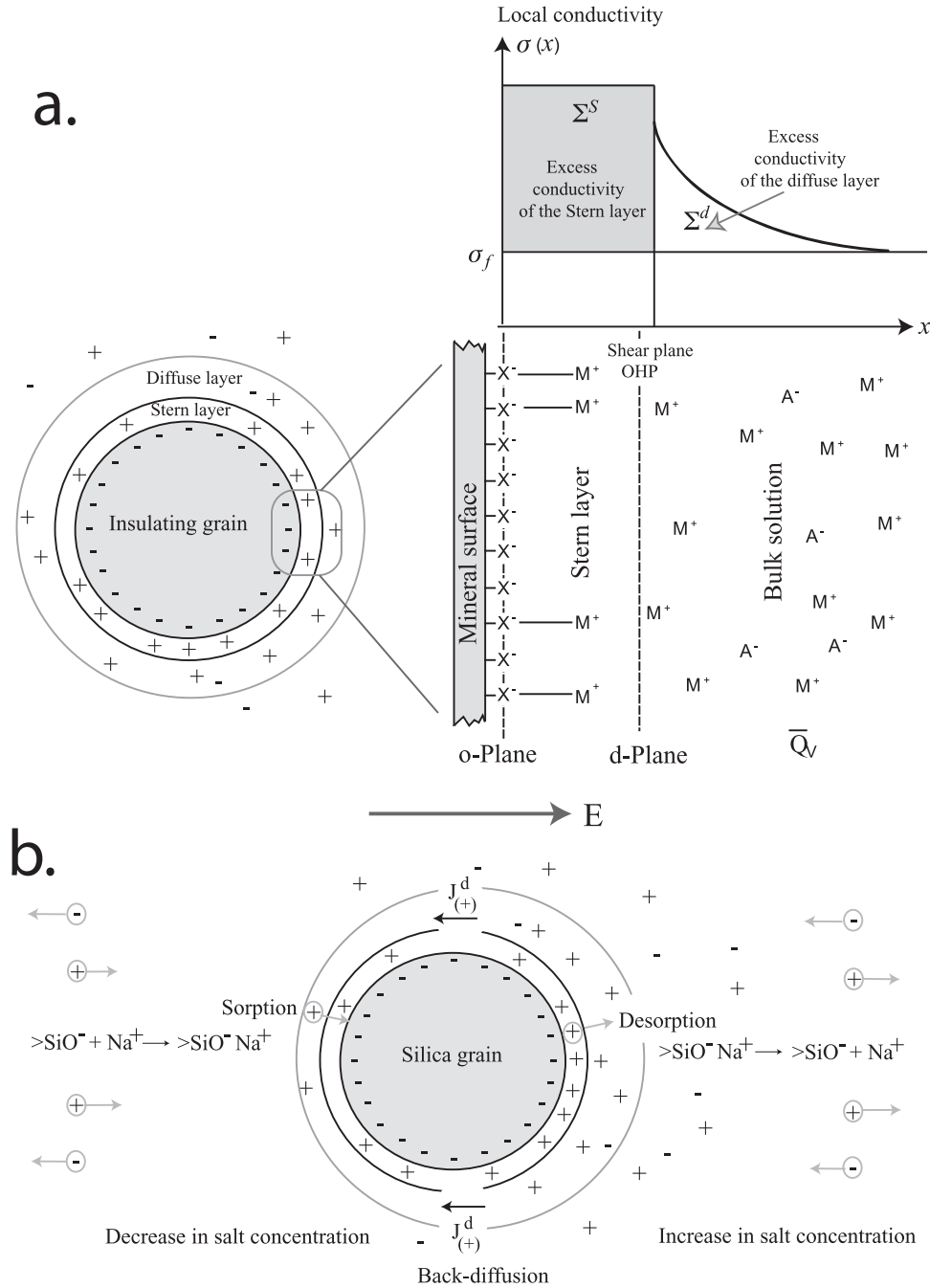
a.

b.

Figure 1. Sketch of the electrical double layer (EDL). (a) The EDL consists of the Stern layer of mobile counterions that are able to move tangentially along the mineral surface and the diffuse layer. The potentials φ_0, φ_d, and φ_β are three triple-layer-model micropotentials, and Σ^S and Σ^d represent the specific surface conductivity (in S) of the Stern and diffuse layers, respectively. (b) Three polarization mechanisms are at play around a grain. The first is the deformation of the diffuse layer because of the electrical field. The second effect is the membrane polarization of neutral salt clouds around the solid particle. The third polarization mechanism is associated with the polarization of the Stern layer (described in Appendix B). The field **E** represents the imposed electrical field, and $\mathbf{J^d}_{(+)}$ represents the back-diffusion flux densities of the counterions of the Stern layer in their surface concentration gradient.

in the salt concentration on the left side of the grain because of the charge transfer by the electrical diffuse layer [e.g., *Dukhin and Shilov*, 2002]. In this case, there is also a back diffusion through the pore space, around the grain, and the diffusion coefficient of the corresponding relaxa-

tion process is the mutual diffusion coefficient of the salt through the pore space. An expression for the mutual diffusion coefficient at the scale of a porous material is given by *Revil* [1999]. In this paper, we neglect this contribution because it seems that this contribution is not dominant in

porous media [*Leroy et al.*, 2008; *Leroy and Revil*, 2009; *Jougnot et al.*, 2010; *Revil and Florsch*, 2010; *Schmutz et al.*, 2010]. However, it should be kept in mind that this assumption is untested.

[10] The relationships between the magnitude of the conductivity $|\sigma|$ and the phase angle φ on one end and the real (in-phase) and imaginary (quadrature) components of the conductivity σ' and σ'' of the complex conductivity σ^* are

$$\sigma^* = |\sigma|\exp(i\varphi) = \sigma' + i\sigma'', \quad (1)$$

$$|\sigma| = \sqrt{\sigma'^2 + \sigma''^2}, \quad (2)$$

$$\tan\varphi = \sigma''/\sigma', \quad (3)$$

where $i = (-1)^{1/2}$ is the pure imaginary number. According to *Leroy et al.* [2008], *Leroy and Revil* [2009], *Jougnot et al.* [2010], *Revil and Florsch* [2010], and *Schmutz et al.* [2010], the main mechanism of polarization in sand at low frequencies (below 100 Hz) corresponds to the polarization of the Stern layer at the pore water–mineral interface (the second contribution mentioned above). We develop here the equations for a porous material having a single polarization scale d_0 (the more general case corresponding to a distribution of polarization scales is discussed in Appendix A and section 5). The microscopic equations for this mechanism are discussed in Appendix B. Under the previous assumptions, the model developed recently by *Revil and Florsch* [2010] can be summarized by the following linear conductivity model:

$$\sigma(\omega) = \frac{1}{F}\left[\sigma_f + (F-1)\sigma_S(\omega)\right], \quad (4)$$

$$\sigma_S(\omega) = \frac{4}{d_0}\left(\Sigma^d + \Sigma^S\right) - \frac{4}{d_0}\frac{\Sigma^S}{1 + i\omega\tau_0}, \quad (5)$$

where $F = \phi^{-m}$ (dimensionless) is the electrical formation factor, ϕ is the connected porosity, m is the cementation exponent, σ_f (in S m^{-1}) is the conductivity of the pore water, $\tau_0 = d_0^2/8D_{(+)}$ is the relaxation time (in s), $D_{(+)}$ is the diffusion coefficient of the counterions of the Stern layer coating the surface of the mineral (related to the mobility by the Nernst-Einstein relationship and expressed in m^2 s^{-1}), Σ^d is the excess of electrical conductivity in the electrical diffuse layer (in S), Σ^S represents the excess of electrical conductivity in the Stern layer (in S), and σ_S (in S m^{-1}) is the equivalent conductivity of the grains coated by the electrical double layer. Equation (5) implies that surface conductivity is characterized by a Debye relaxation mechanism. This means that there is a single relaxation time. However, if the above model is convoluted with the grain size distribution (assumed to be lognormal, for instance), the resulting distribution of relaxation times can be fitted by the empirical Cole-Cole model [*Revil and Florsch*, 2010]. This is discussed in detail in Appendix A and in section 5.

[11] The so-called "surface conductivity" can be decomposed into an in-phase component $\sigma_S'(\omega)$ and a quadrature component $\sigma_S''(\omega)$:

$$\sigma_S'(\omega) = \sigma_S^\infty + \left(\sigma_S^0 - \sigma_S^\infty\right)\frac{1}{1 + \omega^2\tau_0^2}, \quad (6)$$

$$\sigma_S''(\omega) = \left(\sigma_S^0 - \sigma_S^\infty\right)\frac{\omega\tau_0}{1 + \omega^2\tau_0^2}, \quad (7)$$

$$\sigma_S^0 = \frac{4}{d_0}\Sigma^d, \quad (8)$$

$$\sigma_S^\infty = \frac{4}{d_0}\left(\Sigma^d + \Sigma^S\right), \quad (9)$$

where σ_S^0 and σ_S^∞ refer to the low- and high-frequency asymptotic limits of surface conductivity, respectively. It follows that the in-phase conductivity, the quadrature conductivity, and the phase angle are given explicitly by

$$\sigma' = \frac{1}{F}\left\{\sigma_f + (F-1)\left[\sigma_S^\infty + \left(\sigma_S^0 - \sigma_S^\infty\right)\frac{1}{1 + \omega^2\tau_0^2}\right]\right\}, \quad (10)$$

$$\sigma'' = \frac{F-1}{F}\left(\sigma_S^0 - \sigma_S^\infty\right)\frac{\omega\tau_0}{1 + \omega^2\tau_0^2}, \quad (11)$$

$$\varphi = \mathrm{atan}\left[\frac{(F-1)\left(\sigma_S^0 - \sigma_S^\infty\right)\omega\tau_0}{\left(\sigma_f + (F-1)\sigma_S^\infty\right)\left(1 + \omega^2\tau_0^2\right) + (F-1)(\sigma_S^0 - \sigma_S^\infty)}\right], \quad (12)$$

$$\varphi \approx \frac{(F-1)\left(\sigma_S^0 - \sigma_S^\infty\right)\omega\tau_0}{\left[\sigma_f + (F-1)\sigma_S^\infty\right]\left(1 + \omega^2\tau_0^2\right) + (F-1)(\sigma_S^0 - \sigma_S^\infty)}, \quad (13)$$

respectively. Equation (13) corresponds to the first-order Taylor expansion of equation (12), which is valid for a phase smaller than 100 mrad. This assumption is always valid for all the examples treated in this paper, including for distilled water and for most of the field applications. The peak phase is approximately given by $\varphi(\omega = 1/\tau_0) = -2(F-1)\Sigma^S/(d_0\sigma_f)$ (in the limit where surface conductivity can be neglected in the in-phase conductivity), clearly indicating that the peak phase is proportional to the conductance of the Stern layer and inversely proportional to the conductivity of the pore water, as discussed by *Revil and Florsch* [2010]. However, because the Stern layer conductivity depends also on the ionic strength and composition of the pore water, the overall effect may be difficult to separate without the use of an electrical double-layer (triple-layer) model.

[12] The next step, therefore, concerns the connection between the previous macroscopic conductivity model and a chemical speciation model on the mineral surface and its associated electrical double layer (Figure 1). Two choices are possible: either we decide to work at thermodynamic equilibrium or not. Of course, the transport of the ionic species through the porous material occurs outside thermodynamic equilibrium, but if transport is slow enough, speciation can be modeled as a succession of thermodynamic equilibrium states with PHREEQC, for instance. This is a classical standpoint in modeling reactive transport in contaminant plumes, which is correct as long as the

characteristic time of the kinetics of the sorption process is small with respect to the characteristic time of transport. For example, in one of the examples treated below, a salt takes 1000 min (17 h) to move through a column filled with sand. The characteristic time scale for sorption of sodium on the surface of silica is typically a few tens of minutes [*Revil et al.*, 1999a]. In this case, the assumption of thermodynamic equilibrium for the sorption process is valid to first approximation.

[13] The second choice is to model also the kinetics of sorption. We point out that there is no difficulty in coupling our model with a kinetic sorption model (discussed further in section 5), but such kinetic models are not always available. This means also that our induced polarization model could be used to elucidate the kinetics of sorption processes on a mineral surface or a humic substance.

[14] If there is only one type of counterion sorbed onto the mineral surface, the specific surface conductance of the Stern layer is given by [*Revil and Glover*, 1997]

$$\Sigma^S = e z_{(+)} \beta_{(+)} \Gamma^0_{(+)}, \qquad (14)$$

where e represents the elementary charge (taken positive, $e = 1.6 \times 10^{-19}$C), $z_{(+)}$is the valence of the sorbed counterions in the Stern layer (taken positive), $\beta_{(+)}$ is its mobility (in $m^2\ s^{-1}\ V^{-1}$), and $\Gamma^0_{(+)}$ is the surface density of the counterions in the Stern layer (expressed in sites m^{-2}). If the counterion is weakly sorbed, it is safe to consider that its mobility is the same in the Stern layer and in the bulk solution (see a complete discussion by *Revil and Florsch* [2010] and in Appendix B).

[15] For a multicomponent electrolyte, the specific surface conductance in the diffuse layer (in S) is given by

$$\Sigma^d = e \sum_{i=1}^N z_i \beta_i \Gamma^d_i, \qquad (15)$$

where Γ^d_i represents the equivalent surface density of species i in the diffuse layer (in sites m^{-2}), z_i is the valence of species i, and β_i is its mobility ($m^2\ s^{-1}\ V^{-1}$). Considering a classical Gouy-Chapman model and a Boltzman distribution to describe the concentration profiles in the diffuse layer (ideality of the solution is assumed), we have

$$\Gamma^d_i = C^f_i \int_0^{+\infty} \exp\left[-\frac{(\pm 1)z_i e \varphi(\chi)}{k_B T}\right] d\chi, \qquad (16)$$

where T is the temperature (in K), kB is Boltzmann's constant (1.381×10^{-23}J K^{-1}), C^f_i represents the concentration of the species i in the free electrolyte (in mol L^{-1}), (± 1) corresponds to the sign of the charge of the species i, $\varphi(\chi)$ is the local electrical potential (in V) at the distance χ from the mineral surface (in m). To solve analytically the integral of equation (16), we use the following approximation [see *Pride*, 1994, equations 190–194]:

$$\int_0^\infty \exp\left[-\frac{(\pm 1)e z_i \varphi(\chi)}{k_B T}\right] d\chi \approx 2\chi_d \exp\left[-\frac{(\pm 1)e z_i \varphi_d}{2k_B T}\right], \qquad (17)$$

where χ_d is the Debye screening length and φ_d (in V) is the electrical potential at the outer Helmholtz plane (OHP; see Figure 1). Equations (15), (16), and (17) yield

$$\Sigma^d \approx 2\chi_d e \sum_{i=1}^N z_i \beta_i \exp\left[-\frac{(\pm 1)e z_i \varphi_d}{2k_B T}\right], \qquad (18)$$

with z_i taken positive. The Debye screening length is defined by

$$\chi_d = \sqrt{\frac{\varepsilon_f k_B T}{2 I_f 10^3 N_A e^2}}, \qquad (19)$$

where ε_f is the mean permittivity of the diffuse layer, I_f is the ionic strength of the pore water (usually expressed in mol L^{-1}), and N_A is Avogadro's number (6.02×10^{23}mol^{-1}):

$$I_f = \frac{1}{2} \sum_{i=1}^N z_i^2 C_i. \qquad (20)$$

[16] We consider that the mean permittivity of the diffuse layer is equal to the permittivity of the free water ($\varepsilon_f \approx 81\varepsilon_0$, $\varepsilon_0 \approx 8.85 \times 10^{-12}$ F m^{-1}), as discussed by *Pride* [1994]. In this paper, we are interested by the impact upon induced polarization data of Cu^{2+} replacing Na^+ on a silica surface (and vice versa). This implies that we need speciation models for the sorption of both sodium and copper on silica.

2.2. Sorption of Sodium

[17] In this section, we describe an electrical triple-layer model (TLM) to determine the distribution of coions and counterions at the pore water–silica interface in the case of NaCl. The surface mineral reactions at the silanol surface sites in contact with a NaCl electrolyte and their equilibrium constants are reported in Table 1. The surface charge densities (in C m^{-2}) at the surface of the mineral Q_0, in the Stern layer Q_β, and in the diffuse layer Q_s (see Figure 1) can be expressed as

$$Q_0 = e\left(\Gamma^0_{>SiOH_2^+} - \Gamma^0_{>SiO^-} - \Gamma^0_{>SiO^--Na^+}\right), \qquad (21)$$

$$Q_\beta = e\Gamma^0_{>SiO^--Na^+}, \qquad (22)$$

$$Q_s = \sum_{i=1}^N e(\pm 1)z_i\Gamma^d_i, \qquad (23)$$

Table 1. Equilibrium Constants for Surface Complexes[a]

Reactions	Equilibrium Constants
$>SiOH + H^+ \leftrightarrow >SiOH_2^+$	$K_{>SiOH_2^+} = 10^{-2.2}$
$>SiOH \leftrightarrow >SiO^- + H^+$	$K_{>SiO^-} = 10^{-6.2}$
$>SiO^- + Na^+ \leftrightarrow >SiO^-Na^+$	$K_{>SiO^-Na^+} = 10^{-4.5}$
$>SiOH + Cu^{2+} \leftrightarrow >SiOCu^+ + H^+$	$K_{>SiOCu^+} = 10^{-3.4}$
$2>SiOH + Cu^{2+} \leftrightarrow 2(>SiO)^-Cu^{2+} + 2H^+$	$K_{2>SiO^-Cu^{2+}} = 10^{-8.8}$
$>SiOH + SO_4^{2-} + H^+ \leftrightarrow >SiSO_4^- + H_2O$	$K_{>SiSO_4^-} = 10^5$

[a]From *Sverjensky* [2005].

where the notation $>\text{SiO}^-\text{Na}^+$ is used to describe the outer sphere ligand between sodium and the negative silanol site and it shows the negative charge on the o plane and the positive charge on the β plane (see Figure 1a). In the case of a symmetric monovalent electrolyte with a concentration C_f and if concentrations of H^+ and OH^- are small by comparison with the salinity C_f, the ionic strength is equal to the salinity ($I_f = C_f$). This yields the following relationship for the Debye screening length:

$$\chi_d = \sqrt{\frac{\varepsilon_f k_B T}{2 C_f e^2}}. \tag{24}$$

[18] Using equations (16), (17), (23), and (24), the surface charge density in the diffuse layer is given by

$$Q_s = 4\chi_d e C_f \left[\exp\left(-\frac{e\varphi_d}{2k_B T}\right) - \exp\left(\frac{e\varphi_d}{2k_B T}\right)\right], \tag{25}$$

$$Q_s = -\sqrt{8\varepsilon_f k_B T C_f} \sinh\left(\frac{e\varphi_d}{2k_B T}\right). \tag{26}$$

[19] The conservation equation for the surface sites yields

$$\Gamma^0 = \Gamma^0_{>\text{SiOH}} + \Gamma^0_{>\text{SiO}^-} + \Gamma^0_{>\text{SiOH}_2^+} + \Gamma^0_{>\text{SiO}^-\text{Na}^+}, \tag{27}$$

where Γ^0 (in sites m^{-2}) is the total surface site density of the mineral surface (typically around 5 sites nm^{-2} [Carroll et al., 2002; Wang and Revil, 2010]). We use the equilibrium constants associated with the half reactions to compute the surface site densities. Solving equation (27) with the expressions of the equilibrium constants defined in Table 1 yields [Leroy et al., 2008]

$$\Gamma^0_{>\text{SiOH}} = \Gamma^0/A, \tag{28}$$

$$\Gamma^0_{>\text{SiO}^-} = \Gamma^0_{>\text{SiOH}} K_{>\text{SiO}^-} \frac{1}{C_{\text{H}^+} X_0}, \tag{29}$$

$$\Gamma^0_{>\text{SiOH}_2^+} = \Gamma^0_{>\text{SiOH}} K_{>\text{SiOH}_2^+} C_{\text{H}^+} X_0, \tag{30}$$

$$\Gamma^0_{>\text{SiO}^-\text{Na}^+} = \Gamma^0_{>\text{SiOH}} K_{>\text{SiO}^-\text{Na}^+} \frac{C_f X_\beta}{C_{\text{H}^+} X_0}, \tag{31}$$

where

$$A = 1 + K_{>\text{SiO}^-}\frac{1}{C_{\text{H}^+} X_0} + K_{>\text{SiOH}_2^+} C_{\text{H}^+} X_0 + K_{>\text{SiO}^-\text{Na}^+}\frac{C_f X_\beta}{C_{\text{H}^+} X_0}, \tag{32}$$

$$X_0 = \exp\left(-\frac{e\varphi_0}{k_B T}\right), \tag{33}$$

$$X_\beta = \exp\left(-\frac{e\phi_\beta}{k_B T}\right), \tag{34}$$

with φ_0 being the electrical potential (in V) at the o plane corresponding to the mineral surface and φ_β (in V) being

the electrical potential at the β plane corresponding to the plane of the Stern layer (Figure 1). In the case of sodium, we can define the specific surface conductances in the Stern layer and the diffuse layer from equations (14) and (18),

$$\Sigma^S = e\beta_{\text{Na}^+}\Gamma^0_{>\text{SiO}^-\text{Na}^+}, \tag{35}$$

$$\Sigma^d \approx 2\chi_d e C_f 10^3 N_A \left[\beta_{\text{Na}^+}\exp\left(-\frac{e\varphi_d}{2k_B T}\right) + \beta_{\text{Cl}^-}\exp\left(\frac{e\varphi_d}{2k_B T}\right)\right]. \tag{36}$$

[20] The mobility of the sodium in the Stern layer is assumed to be the same as in the bulk pore water because sodium forms a weak complex with the silica surface (see discussion in Appendix B). Note that our model does not account for the sorption of chloride that occurs at very low pH values (below the isoelectric point). For very low pH values (below 3), we expect chloride to play a dominant role in the polarization of the Stern layer around the grains. This will be investigated in a future publication.

2.3. Sorption of Copper

[21] The speciation model for a copper sulfate solution in thermodynamic equilibrium with a silica surface and the values of the equilibrium constants are given in Table 1. The complexation model is taken from Schindler et al. [1976] and is shown in Figure 2. The equilibrium constants for leading reactions in the aqueous solution of copper sulfate are given in Table 2. Here we assume that in the case of the monodentate binding sites, copper ions are sorbed as an inner sphere ligand. Conversely, bidentate complexation between copper and the silica surface occurs as an outer sphere ligand (Figure 2). Consequently, there are strong differences between the different complexation behaviors between silica and Na$^+$ (being loosely absorbed), while Cu^{2+} forms rather strong complexation with both inner (monodentate) and outer sphere (bidentate) bondings. We will see that this has strong implications regarding the phase lag between the electrical field and the electrical current. Consequently, the surface charge density Q_0 (in C m^{-2}) at the surface of the minerals (see Figure 2) can be expressed as

$$Q_0 = e\left(\Gamma^0_{>\text{SiOH}_2^+} + \Gamma^0_{>\text{SiOCu}^+} - \Gamma^0_{>\text{SiO}^-} - 2\times\Gamma^0_{2>\text{SiO}^-\text{Cu}^{2+}} - \Gamma^0_{>\text{SiSO}_4^-}\right), \tag{37}$$

where Γ^0_i is the surface density species i (in sites m^{-2}). The surface charge density Q_β in the Stern layer is determined according to

$$Q_\beta = 2e\Gamma^0_{2>\text{SiO}^-\text{Cu}^{2+}}. \tag{38}$$

[22] Following the same steps as used in section 2.2, we can compute the surface charge density in the diffuse layer in the case of a symmetrical bivalent electrolyte as follows:

$$Q_s \approx -\sqrt{8\varepsilon_f k_B T C_f} \sinh\left(\frac{e\varphi_d}{k_B T}\right). \tag{39}$$
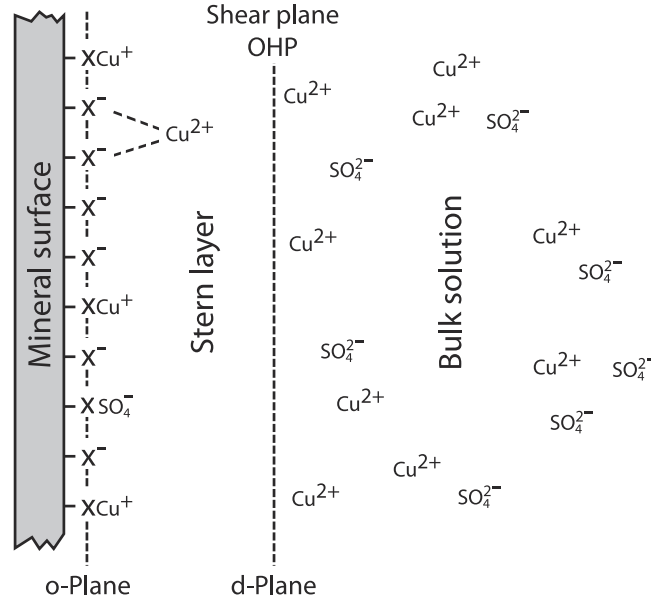
Figure 2. Sketch of the electrical double layer showing the speciation of copper and sulfate for a solution of copper sulfate in contact with a silica surface. Sorption of copper on the mineral surface (inner sphere ligand) occurs as a monodentate complex (immobile), while sorption in the Stern layer (outer sphere ligand) occurs as a (mobile) bidentate complex.

[23] The conservation equation for the surface sites yields

$$\Gamma^0 = \Gamma^0_{>SiOH} + \Gamma^0_{>SiO^-} + \Gamma^0_{>SiOH_2^+} + \Gamma^0_{>SiOCu^+} + \Gamma^0_{2>SiO^-Cu^{2+}} \\ + \Gamma^0_{>SiSO_4^-}. \tag{40}$$

[24] Solving equation (40) with the expressions of the equilibrium constants defined through the reactions displayed in Table 1 yields

$$\Gamma^0_{>SiOH} = \frac{-b + \sqrt{b^2 - 4ac}}{2a}, \tag{41}$$

with the following expressions for the parameters a, b, and c:

$$a = 2K_{2>SiO^-Cu^{2+}},$$
$$b = 1 + \frac{K_{>SiO^-}}{C_{H^+}X_0} + K_{>SiOH_2^+}C_{H^+}X_0 + \frac{K_{>SiOCu^+}C_{Cu^{2+}}X_0}{C_{H^+}} + \frac{K_{>SiSO_4^-}C_{SO_4^{2-}}C_{H^+}}{X_0}, \tag{42}$$
$$c = -\Gamma^0,$$

$$\Gamma^0_{>SiO^-} = \Gamma^0_{>SiOH}K_{>SiO^-}\frac{1}{C_{H^+}X_0}, \tag{43}$$

$$\Gamma^0_{>SiOH_2^+} = \Gamma^0_{>SiOH}K_{>SiOH_2^+}C_{H^+}X_0, \tag{44}$$

$$\Gamma^0_{>SiOCu^+} = \Gamma^0_{>SiOH}K_{>SiOCu^+}\frac{C_{Cu^{2+}}X_0}{C_{H^+}}, \tag{45}$$

$$\Gamma^0_{2>SiO^-Cu^{2+}} = \left(\Gamma^0_{>SiOH}\right)^2 K_{2>SiO^-Cu^{2+}}\frac{C_{Cu^{2+}}}{C_{H^+}^2}, \tag{46}$$

$$\Gamma^0_{>SiSO_4^-} = \Gamma^0_{>SiOH}K_{>SiSO_4^-}\frac{C_{SO_4^{2-}}C_{H^+}}{X_0}. \tag{47}$$

[25] The following specific surface conductances of the Stern and diffuse layers can be defined from equations (14) and (18):

$$\Sigma^S = 2e\beta_{Cu^{2+}}\Gamma^0_{2>SiO^-Cu^{2+}}, \tag{48}$$

$$\Sigma^d \approx 4\chi_d e C_f 10^3 N_A \left[\beta_{Cu^{2+}}\exp\left(-\frac{e\varphi_d}{k_B T}\right) + \beta_{SO_4^{2-}}\exp\left(\frac{e\varphi_d}{k_B T}\right)\right], \tag{49}$$

respectively. The mobility of copper in the Stern layer may be smaller than in the bulk because of the strong sorption

Table 2. Equilibrium Constants for Leading Reactions in the Aqueous Solution of Copper Sulfate[a]

Reaction	Equilibrium Constant
$H_2O \leftrightarrow H^+ + OH^-$	10^{-14}
$Cu^{2+} + H_2O \leftrightarrow CuOH^+ + H^+$	10^{-8}
$Cu^{2+} + 2H_2O \leftrightarrow Cu(OH)_2 + 2H^+$	$10^{-13.7}$

[a]From *Schindler et al.*[1996].

of these counterions on silica. However, to stay conservative, we take the same value as in the bulk pore water. Note that our model does not account for the sorption of sulfate in the Stern layer. For the environmental conditions used in our study, there is no evidence for the existence of such a complex. In some other conditions, the sorption of sulfate would need to be explicitly accounted for.

2.4. Numerical Resolution of the Problem

[26] The electrical potentials of the TLM are related by [*Hunter*, 1981]

$$\varphi_0 - \varphi_\beta = Q_0/C_1 , \qquad (50)$$

$$\varphi_\beta - \varphi_d = -Q_s/C_2 , \qquad (51)$$

where C_1 and C_2 (in F m^{-2}) are the integral capacities of the inner and outer parts of the Stern layer, respectively. Typically, we can use $C_1 = 1.0$ F m^{-2} and $C_2 = 0.2$ F m^{-2}

[*Carroll et al,*. 2002; *Wang and Revil*, 2010]. The global electroneutrality equation for the mineral-water interface is

$$Q_0 + Q_\beta + Q_s = 0 . \qquad (52)$$

[27] The brines are assumed to be completely dissociated in water, and we neglect the dissolution of silica in the pore water.

[28] The previous complexation problem cannot be solved directly to compute the different potentials and charge densities. We use a quasi-Newton scheme [see *Tarantola*, 2005] to solve equations (34)–(36) and to obtain potentials in the different planes. We start the optimization with prior values of the electrical potentials to compute the surface charge densities using equations (21), (26), and (28)–(31) in the case of a NaCl solution and equations (37)–(49) in the case of a CuSO$_4$ solution. The electrical potentials are optimized step by step. Once convergence has been reached, the microscopic electrical potentials of the electrical double layer are obtained, then all the surface charge densities and the surface site densities are determined, and finally, the values of the specific surface conductances Σ^d and Σ^S are computed.

3. Materials and Methods

3.1. Experimental Setup

[29] The column (made of an inert plastic) used for our experiments is shown in Figure 3. The column was filled
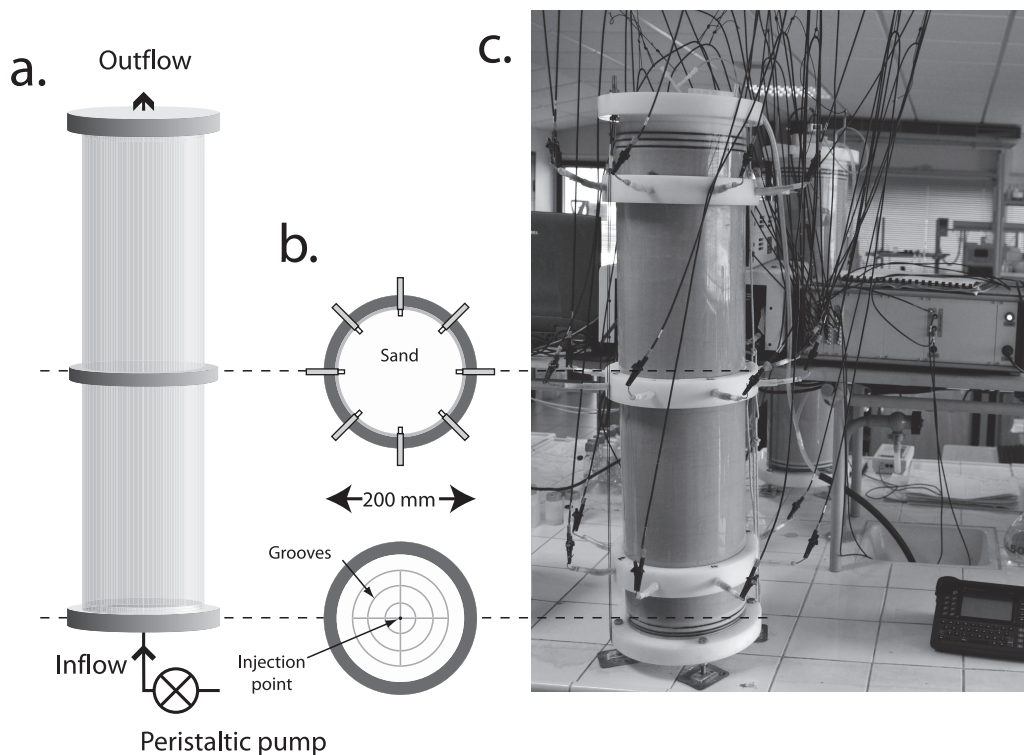

Figure 3.   Sketch of the column used to perform the first set of experiments. (a) Side view. The height of the column is 800 mm. (b) Cross sections of the inflow and the electrode array located in the middle of the column. (c) Picture of the laboratory column and SIPLab II equipment used to measure the complex resistivity.

with a Fontainebleau sand (type Ga39, 98% silica, well-sorted and well-rounded grains with a mean grain diameter $d_0 = 100 \pm 10$ μm). Care was taken to compact the sand homogeneously during the infilling of the column with the sand. Once the column was filled, it was saturated with CO_2 and then saturated by degassed water to avoid entrapped air. The entry of the column was manufactured in such a way that the brine entering the column from the bottom did not produce fingering. The flux of the solution entering the column was imposed by a peristaltic pump. The flow was constant (flow rate of 5 mL min^{-1}), and the velocity of the water was on the order of 2.7×10^{-5} m s^{-1}. The hydraulic conductivity K of the sand packed in the column was independently measured at different imposed hydraulic heads and was equal to 2.8×10^{-5} m s^{-1}. The measured total connected porosity is equal to 0.40. The pH of the solution is between 4.5 and 6 because of the dissolution of CO_2 in the pore water (e.g., see calculations by *Revil et al.* [1999a]). A salt advection experiment was performed to determine the effective (mobile) porosity ($\phi_{eff} = 0.31$) and the longitudinal dispersivity (1.6×10^{-3} m). According to *Revil and Cathles* [1999], the effective porosity is approximately equal to the inverse of the electrical formation factor F. This is approximately the case here as $1/\phi_{eff} = 3.2$, and we will see in section 4 that the formation factor is 3.1.

[30] The spectral induced polarization measurements were made with the SIPLab II equipment developed by Radic Research (http://www.radic-research.homepage.t-online.de/default.html). This apparatus measures the magnitude of the conductivity and the phase lag from 1 mHz to 12 kHz. The sand column was instrumented with 24 nonpolarizable electrodes of Cu/CuSO$_4$. The contacts between the electrodes and the sand of the column were made with porous cylinders with a length of 20 mm and a diameter of 6 mm. Eight electrodes were located at equal distances along a circle in the middle of the column (Figures 3 and 4). The cables connecting the electrodes and the impedance meter were separated as much as possible from each other to minimize electromagnetic couplings, which typically occur at high frequencies (e.g., above 100 Hz or higher).

[31] Each measurement is performed with four electrodes (two are used to inject the current, and two are used to measure the electrical potential). Several choices are possible to perform the measurements, as shown in Figure 4. In order to make a good choice, we studied the sensitivity of the measurements for four distinct arrays using the analytical solutions given by *Zhou* [2007]. This sensitivity analysis is done assuming a homogeneous resistivity distribution. The results are shown in Figure 4. The array labeled setup 1 has a more or less homogeneous sensitivity inside a cross section of the column, while setup 2 has a strong sensitivity only close to the electrodes. The arrays corresponding to setups 3 and 4 have sensitivities only near the outer boundary of the column. Consequently, we used the array corresponding to setup 1 to perform our measurements. The raw measurements are the impedance and the phase lag. A geometrical factor for the middle array is 0.83 m. This geometrical factor is used to convert the measured impedances to resistivities or conductivities.

[32] Spectra of the resistivity and the phase angle were carried out in the range 45 mHz to 12 kHz, with measure-
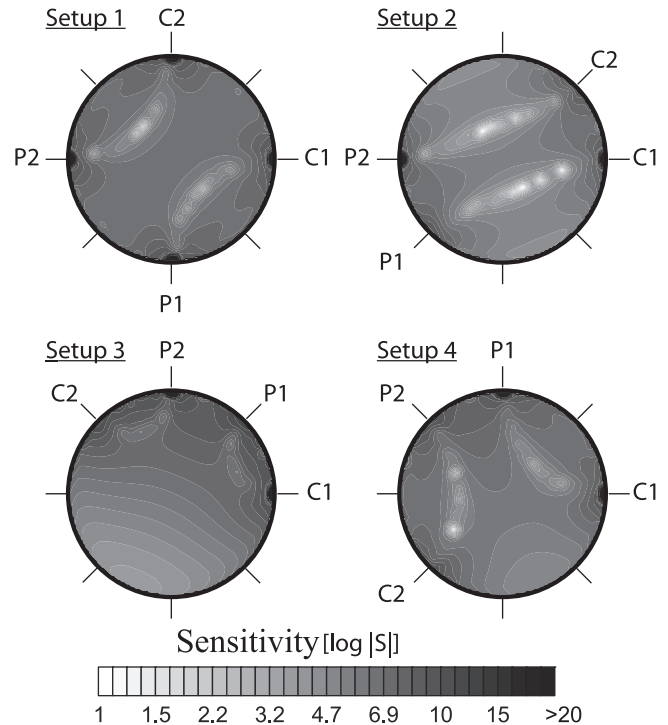

Figure 4. Sensitivity of the electrode arrays and phase spectra. Absolute values of the sensitivity of the resistivity obtained through a column section for four setups of electrodes for injection (C1 and C2) and for measure of potential (P1 and P2) are shown. Setup 1 was chosen because it has a uniform sensitivity at a given depth in the column.

ments performed at 19 frequencies. Reciprocal measurements were always performed (for the reciprocal measurements, the potential electrodes were simply exchanged with the current electrodes). Reciprocity was a way to estimate data quality; good reciprocity in spectral induced measurements is often considered as a way to check that there is no residual polarization of the electrodes [*Binley et al.*, 1996; *Chambers et al.*, 2004; L. Slater, personal communication, 2009]. These reciprocal measurements were used to estimate the data quality, and the uncertainty on the phase was generally found to be below 0.2 mrad. The measurements were reproducible. A typical example of two spectra obtained for sodium and copper is shown in Figure 5.

[33] The pore water was sampled in the middle of the column, so the induced polarization measurements reported below are taken at the middle of the column. Sampling the pore fluid was performed with a membrane connected to a capillary. The pore water was pumped with a syringe. Chloride and sulfate concentrations were analyzed by chromatography with a Dionex DX120 and a column AS9-HC. The concentration of copper was determined by colorimetry after reaction with ammonia, with a wavelength of 640 nm.

3.2. Experimental Procedure

[34] Two sets of experiments were performed. A sand column experiment was first performed to see the change in the complex conductivity during the advective transport of a copper sulfate solution replacing a sodium chloride
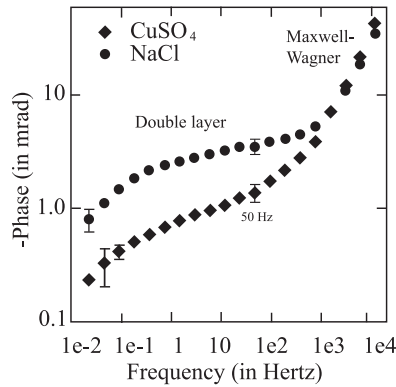
Figure 5. Phase versus frequency for the sand saturated by solutions of NaCl and CuSO₄ at 210 μS cm⁻¹. At high frequencies (>100 Hz), the polarization response is dominated by the Maxwell-Wagner polarization, while at lower frequencies (<100 Hz), the polarization response is dominated by the polarization of the electrical double layer, as shown by *Leroy et al.* [2008]. Reciprocity is checked over the entire frequency range investigated in our study (20 mHz to 12 kHz; <0.4% for the resistivity and <0.2 mrad for the phase). The error bars are only shown when they are larger than the size of the symbols.

solution (Figure 6). Before the beginning of the experiment at $t = 0$ s, the sand was washed with demineralized water for several days. The electrical conductivity of the demineralized water was less than 5 μS cm⁻¹ at 25°C. Then, at $t = 0$ min, we started to flush the column with a NaCl solution with an electrical conductivity of 220 μS cm⁻¹ (at 25°C). This corresponds to phase I in Figure 6. Once the electrical conductivity of the electrolyte at the outlet of the column was stabilized, we started to inject a solution of CuSO₄ at the same conductivity (220 μS cm⁻¹ at 25°C) from the bottom of the column. This corresponds to phase II in Figure 6. Then, a NaCl solution was flushed through the column with an electrical conductivity equal to 410 μS cm⁻¹ (phase III). Finally, a CuSO₄ solution was flushed through the column with an electrical conductivity equal to 410 μS cm⁻¹ (see Figure 6). The compositions of the solutions used during each phase are reported in Table 3.

[35] The magnitude of the complex resistivity and the phase shift between the current and the voltage were measured with a sampling rate of one measurement per quadripole every 60 min. The pore water samples taken for the chemical analysis from the column correspond to 3 mL. This volume is extracted slowly over 4 min in order to not disturb the flow of the pore water in the column. These samples are taken every 20 min. In addition to chemical analysis, we also modeled the reactive transport in the sand column with the numerical code PHREEQC [*Parkhurst and Appelo*, 1999].

[36] A second set of experiments was performed with both sodium chloride and copper sulfate solutions in a broad range of salinities at thermodynamic equilibrium with the same sand at the same state of compaction. The following conductivities were used at 25°C with NaCl: 100, 210, 320, 420, and 550 μS cm⁻¹. The conductivities used with the CuSO₄ solutions were 110, 210, 320, 410,

and 510 μS cm⁻¹. Thermodynamic equilibrium was considered to be obtained when the phase lag reached a plateau (typically after several days).

4. Experimental Results

[37] We performed a total of 866 measurements during the first set of experiments (433 normal and 433 reciprocal measurements). The experiment lasted 9 days. Reciprocity was checked to 0.2% for the resistivity and 0.05 mrad for the phase. In order to observe the behavior of induced polarization measurements during the advection of the copper sulfate solution, we plotted the magnitude and the phase angle at 183 mHz (Figures 6−10). This frequency is close to the peak frequency $f_{\text{peak}} \approx 4D_{(+)}/(\pi d_0^2)$ of the complex resistivity spectra for both NaCl and CuSO₄ solutions. Using $d_0 = 100$ μm and $D_{(+)} = 1.32 \times 10^{-9}$ m² s⁻¹ for Na⁺, the location of the loss peak f_{peak} occurs at ⌐168 mHz, while for Cu²⁺, $D_{(+)} = 7.10 \times 10^{-10}$ m² s⁻¹ (see Table 4), we find $f_{\text{peak}} \approx 90$ mHz. These loss peaks are close to the observed frequency peaks at 204 and 110 mHz, respectively.

[38] In phase I, the resistivity and the phase decrease from 3200 to 180 Ωm and from about 60 to 3 mrad, respectively. In the transition between phases I and II, no significant change in the resistivity was observed, with the exception of a small transient change in the resistivity from 180 to 190 Ωm when the chloride concentration decreases and the sulfate concentration increases (see Figure 8). These changes are very well reproduced by the numerical model as discussed further below. The value of the absolute phase decreases sharply from 3 to 0.5 mrad during the transition from phase I to phase II, and then the decay is smaller over time.

[39] In the transition between phases II and III, the electrical conductivity of the brine increases from 220 to 410 μS cm⁻¹, and sodium replaces copper as the main cation in the pore water. This results in a decrease of the bulk resistivity of the sand from 180 to 95 Ωm. The phase angle decreases from 0.5 to 0.3 mrad, and then it goes back to 0.5 mrad.

[40] In the transition from phase III to phase IV, the sodium chloride solution is replaced by a copper sulfate solution at the same electrical conductivity. The resistivity remains stable during the transition at around 95 Ωm (there is actually a small transient at 105 Ωm when concentration of chloride decreases and the concentration in sulfate increases). The absolute value of the phase decreases from 0.5 to less than 0.2 mrad.

[41] For both salts (NaCl and CuSO₄), the resistivity is equal to 180 Ωm with a conductivity of the electrolyte at 200 μS cm⁻¹, and it is close to 95 Ω m with a conductivity of the electrolyte at 400 μS cm⁻¹. The bulk conductivity of the material arises from two processes. One is related to the bulk pore water conductivity, and the other is the surface conductivity along the pore water−mineral interface. The sorption of copper would modify the surface conductivity. Therefore, if the modulus of the resistivity does not depend on the presence of copper (it depends only on the value of the conductivity of the pore water solution), this means that the contribution of surface conductivity to the overall conductivity of the porous material is very small.
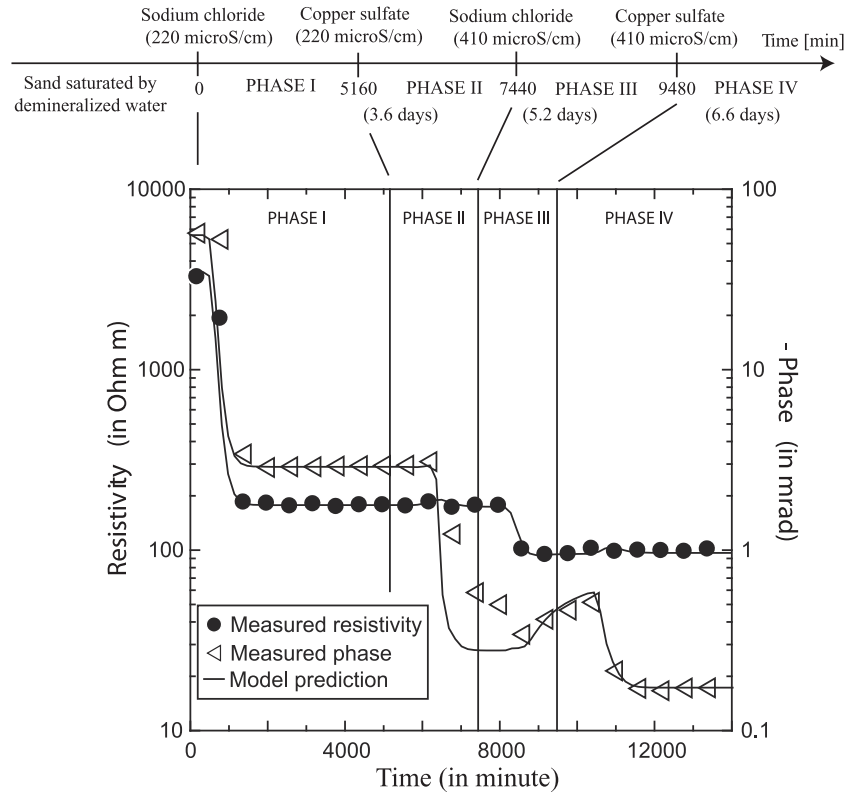
Figure 6. Time sequence of the first experiment at 183 mHz. The sand was initially saturated with de-mineralized water. At $t = 0$ min, a solution of NaCl is flushed from the bottom of the column with an electrical conductivity of 220 μm cm^{-1}. At $t = 5160$ min, a solution of copper sulfate is flushed from the bottom of the column at the same conductivity as the sodium chloride solution. At $t = 7440$ min, a solution of sodium chloride is flushed through the column with an electrical conductivity of 410 μS cm^{-1}. At $t = 9480$ min, a solution of CuSO$_4$ is flushed through the column with an electrical conductivity of 410 μS cm^{-1}. The measurements are made at the middle of the column, which explains the delay between the injection and the change in the resistivity and the phase. The lines are the results of the modeling of the phase and the resistivity during transport (see Table 6).

From equations (2) and (10), the in-phase conductivity is given by

$$\sigma \approx \frac{1}{F}\left[\sigma_f + \frac{4(F-1)}{d_0}\left(\Sigma^d + \Sigma^S\right)\right]. \qquad (53)$$

[42] We use the slope of the linear fit shown in Figure 11 to determine the formation factor of the sand. This yields $F = 3.1 \pm 0.1$. This is consistent with Archie's law, with a porosity of 0.42 and a cementation exponent $m = 1.3$. The value of this cementation exponent is somewhat smaller than predicted by differential effective medium theory for a pack of spherical particles ($m = 1.5$ [see *Sen et al.*, 1981]),

Table 3. Characteristics of the Solutions Injected During the Experimentation[a]

Solution	$C_f (10^{-3}$ mol L$^{-1})$	pH
NaCl 220 μS cm^{-1}	1.6	6
NaCl 410 μS cm^{-1}	3.2	6
CuSO$_4$ 220 μS cm^{-1}	0.9	5
CuSO$_4$ 410 μS cm^{-1}	1.8	5

[a]These characteristics are also used in the triple layer model (TLM) to compute the phase angles.

but consistent with data in the literature. Regarding surface conductivity, taking $F = 3.1$, $d_0 = 100$ μm, and an overall specific surface conductivity of 1×10^{-8} S yields a surface conductivity contribution equal to $\sim 3 \times 10^{-4}$ S m^{-1}. This indicates that the surface conductivity contribution to the in-phase conductivity is negligible. Therefore, the in-phase conductivity can be approximated by

$$\sigma' \approx \frac{1}{F}\sigma_f. \qquad (54)$$

[43] The first lesson learned from these experiments concerns the sensitivity of the phase to the presence of copper. This means that the DC resistivity method widely used in the field to map contaminant plumes can be totally blind to the presence of copper if there is no change in the ionic strength of the pore water. As discussed above, the phase lag is, on the other hand, more sensitive to the presence of a contaminant such as copper. This shows the superiority of induced polarization over DC resistivity to map this type of contaminant in the ground. In the field, one can expect a sensitivity of 0.1 mrad with true 24 bit systems with timing of 60 ps at 1 kHz (G. Olhoeft, personal communication, 2010). For very extreme and unfavorable conditions, *Grimm et al.* [2005] had a sensitivity of 0.8 mrad.
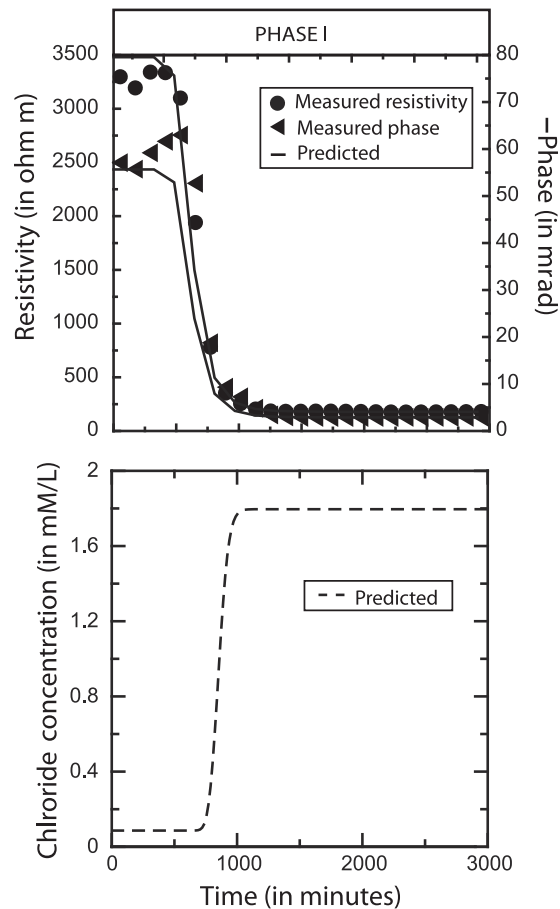
Figure 7. Evolution of the resistivity, the phase angle, and the chloride concentration during the transition between the initial stage for which the sand is saturated by demineralized water (DW) and phase I of the experiment, corresponding to the flushing of a sodium chloride solution from the bottom of the column. The dashed line corresponds to the chemical modeling of the concentrations with the reactive transport model with PHREEQC. The solid lines are the results of the modeling of the phase and the resistivity during transport. The resistivity and the phase angle are measured at 183 mHz in the middle of the column.

5. Comparison Between Theory and Experiments

5.1. Influence of the Chemistry Near the Relaxation Frequency

[44] Using the macroscopic conductivity model and the TLM approach described in section 2, we compute the theoretical values of the phase lag at a frequency of 183.1 mHz for 10 solutions used to saturate our silica sand. The characteristics of these solutions are reported in Table 5, predictions from the triple-layer models are reported in Table 6, and the computed phase lags are reported in Table 7. A comparison between the theoretical and measured values of the phase lags is shown in Figure 12. The equilibrium constants used for the sodium are taken directly from *Sverjensky* [2005]. To our knowledge, there is no model in the

literature able to explain the sorption of copper on silicate with a triple-layer model. *Subramaniam et al.* [2003] provide a model, but the agreement between the predictions of this model and experimental data is not very good. We therefore decided to use a model similar to the one developed by *Phan et al.* [2004] for the sorption of zinc. The model predicts positive values for the diffuse layer potential in the case of copper and negative values in the case of sodium. This is qualitatively in agreement with published experimental data in the cases of copper and sodium. This type of model explains both the monitoring of the concentration of copper and the spectral induced polarization response during the transport. Figure 12 shows a quite good agreement between the prediction of the spectral induced polarization model (coupled with the complexation and triple-layer models) and the measurements. This means, in turn, that complex resistivity or induced polarization is sensitive to the complexation on the mineral surface in a way that can be quantitatively predicted.

[45] We have not discussed the effect of the pH on the phase at this point. The pH of the NaCl and $CuSO_4$ solutions are close to 5.3 and 4.5 (Table 5), respectively. Our solutions are slightly acidic because of the dissolution of CO_2 and the subsequent dissociation of carbonic acid in the pore water. This can be reproduced assuming that carbonic acid dissociates to protons and HCO_3^- and the secondary dissociation of the bicarbonate ion was neglected. The resulting pore water pH is 5.4. As shown in Table 1, a proton is a determining species of the surface charge of silica, and therefore, the polarization behavior is based upon this. It is therefore legitimate to wonder how the change in pH affects the change of phase. Our simulations show that the pH effect (1 pH unit in the range 5−6) upon the phase is a much smaller effect than the effect of ion exchange. This was also experimentally proven by *Lesmes and Frye* [2001] using a Berea sandstone.

[46] For the first set of experiments, our model predicts very well the conductivity and the phase for all the experiments (see Figure 6). For instance, when demineralized water was used (Figure 6), we obtained a measured phase of −55 ± 5 mrad. The value of the peak phase is approximately given by $-2\Sigma^S(F-1)/(d_0\sigma_f)$. Taking $F = 3.1$, $d_0 = 100\ \mu m$, and $\sigma_f = 3\ \mu S\ cm^{-1}$ yields a specific surface conductivity of $(0.4 \pm 0.2) \times 10^{-9}$ S, in agreement with *Revil and Florsch* [2010, Figure 12]. Our model predicts the phase lag accurately except when copper is replaced by sodium (see Figure 6). This is because our model assumes thermodynamic equilibrium, whereas the kinetics of the replacement of copper by sodium is slow and thermodynamic equilibrium is not reached in phase III.

[47] The explanation of the observed phase differences between Na and Cu relies on their different complexation behaviors, with Na being loosely absorbed [*Carroll et al.*, 2002], while Cu forms relatively strong (less mobile) complexation with both inner (monodentate) and outer sphere (bidentate) bondings. If Cu is an inner sphere ligand, it is difficult for sodium to replace copper in phase IV. In addition, because copper is a divalent cation, it can be responsible for a reversal in the electrostatic potential of the diffuse layer (see Table 6). As a result, Na ions in the bulk fluid can be strongly excluded from the diffuse layer. How are these sodium cations to replace Cu in the Stern layer if they
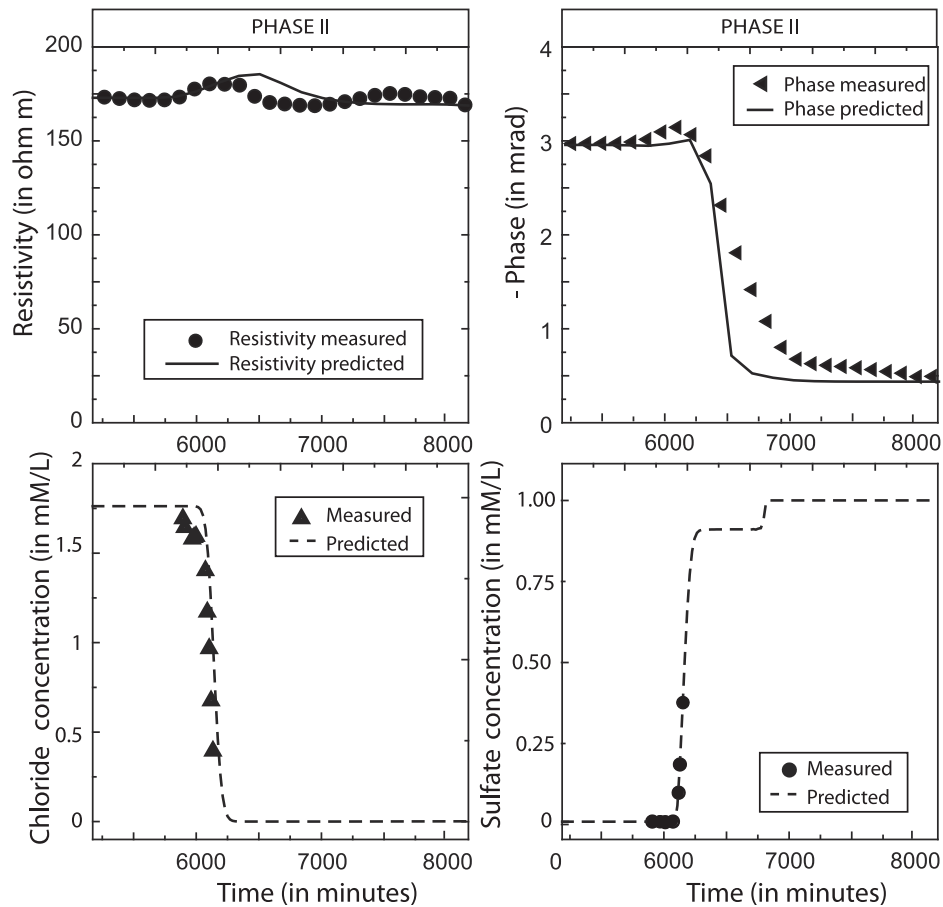
Figure 8. Evolution of the resistivity, phase angle (uncertainty <0.2 mrad), and chloride and sulfate concentrations during the transition between phase I (flushing of a NaCl solution) and phase II (flushing of a $CuSO_4$ solution). The dashed lines correspond to the chemical modeling of the concentrations with the reactive transport model with PHREEQC. The solid lines are the result of the modeling of the phase lag and the resistivity during transport. The resistivity and the phase angle are measured at 183 mHz at the middle of the column.

cannot get easily into the diffuse layer? The slow and incomplete replacement of Cu with Na in phase IV of the first set of experiments can be seen in Figure 6. This then indicates that induced polarization may have the ability to follow the kinetics of such slow sorption processes at the surface of the mineral. Obviously, additional experimental results are needed to validate the present induced polarization model, but it appears promising as a nonintrusive (geophysical) spectroscopic tool to study sorption processes on mineral surfaces.

[48] The second set of experiments (performed at thermodynamic equilibrium) is very well predicted by our model, as shown in Figure 12. The model is seen to predict well both the conductivity and the phase lag for a broad range of salinities. In turn, this means that the Stern layer polarization is likely to be the dominant polarization mechanism in sands.

5.2. Modeling Spectral Induced Polarization Over the Entire Low-Frequency Spectrum

[49] To explain the induced polarization response in the complete spectrum of frequencies, we have to account for two additional points: the first concerns the distribution of the polarization length scales (and its influence upon the

distribution of relaxation times; see Appendix A), and the second concerns the Maxwell-Wagner polarization.

[50] The distribution of polarization length scales is always broader than simply predicted by the grain size distribution, as discussed in detail by *Leroy et al.* [2008]. *Leroy et al.* [2008] have demonstrated experimentally that the roughness of the grains is responsible for a broad distribution of polarization length scales (bounded in size by the grain sizes). These polarization length scales are responsible for polarization losses occurring in between the main relaxation frequency discussed above and related to the main grain size and the Maxwell-Wagner polarization occurring at higher frequencies (see Figure 5). It is customary to observe a plateau in the magnitude of the phase for this frequency band [*Vinegar and Waxman*, 1984], a decrease of the magnitude of the phase below the relaxation frequency $1/\tau_0$ discussed in section 4 (and associated with the mean of the grain size distribution), and an increase of the magnitude of the phase when the Maxwell-Wagner polarization starts to dominate the IP response [*Leroy et al.*, 2008]. Fourier and fractal grain shape analysis has been applied to characterize the surface irregularities of sand grains [*Hyslip and Vallejo*, 1997; *Drolon et al.*, 2003]. If
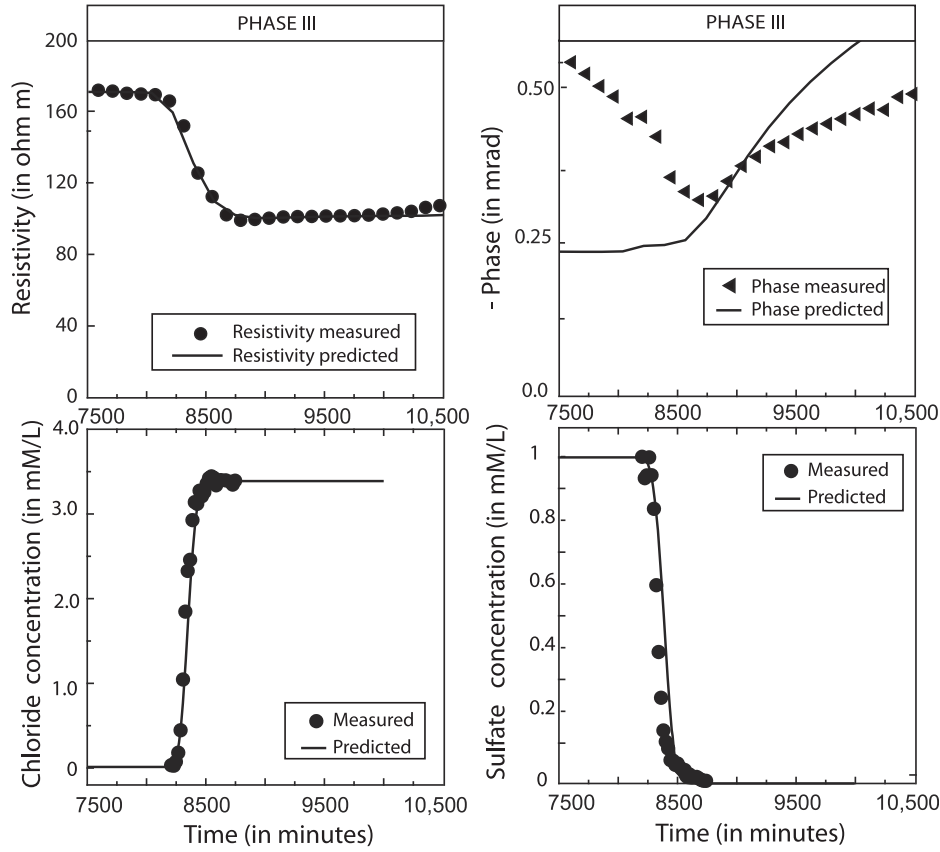
Figure 9. Evolution of the resistivity, phase angle (uncertainty <0.2 mrad), and chloride and sulfate concentrations during the transition between phase II (flushing of a CuSO$_4$ solution) and phase III (flushing of a solution NaCl solution). The dashed lines correspond to the chemical modeling of the concentrations with the reactive transport model with PHREEQC. The solid lines are the results of the modeling of the phase and the resistivity during transport. The resistivity and the phase angle are reported at 183 mHz.

these surface irregularities are associated with polarization length scales, this means that there is a broad distribution of relaxation times, the largest relaxation times being limited by those associated with the size of the grains themselves. The idea that the surface roughness of the particles affects the complex conductivity of porous materials is not new. It has been proposed, for instance, by *Bordi et al.* [1993] and *Cametti et al.* [1995] in their studies on the Maxwell-Wagner polarization of human lymphocyte suspensions in NaCl solutions of varying salinities. *Le Méhauté and Crépy* [1983] and *Wong* [1987] have proposed models connecting the fractal dimensions of the mineral surface to the low-frequency complex conductivity of sedimentary rocks. In material science, constant phase elements are used extensively in equivalent electrical circuits for fitting impedance data, and this behavior is generally attributed to surface roughness [*McDonald*, 1987].

[51] To model the entire frequency spectrum investigated experimentally, we need to include not only the influence of the low-frequency polarization mechanisms associated with charge accumulations at polarization length scales but also true dielectric polarization mechanisms such as the Maxwell-Wagner polarization. The complex effective conductivity and the apparent phase lag of the porous material are now given by [*de Lima and Sharma*, 1992]

$$\sigma^*(\omega) = \sigma_{\text{eff}}(\omega) + i\omega\varepsilon_{\text{eff}}(\omega),\tag{55}$$

$$\varphi = \operatorname{atan}\left[\frac{\omega\varepsilon_{\text{eff}}}{\sigma_{\text{eff}}}\right],\tag{56}$$

respectively, where the effective conductivity and the effective permittivity are defined by [see *Leroy and Revil*, 2009, Appendix A]

$$\sigma_{\text{eff}}(\omega) = \operatorname{Re}[\sigma^*(\omega)],\tag{57}$$

$$\varepsilon_{\text{eff}}(\omega) = \operatorname{Im}[\sigma^*(\omega)/\omega].\tag{58}$$

[52] In equations (57) and (58), Re[ ] and Im[ ] represent the real and imaginary components of the complex number in the argument. The effective complex conductivity is given by

$$\sigma^*(\omega) = \frac{1}{F}\left[\sigma_f^* + (F-1)\sigma_S^*(\omega)\right],\tag{59}$$

where we have included the discontinuity of the current displacement at the interface between the different phases of the porous composite [see *Leroy and Revil*, 2009,
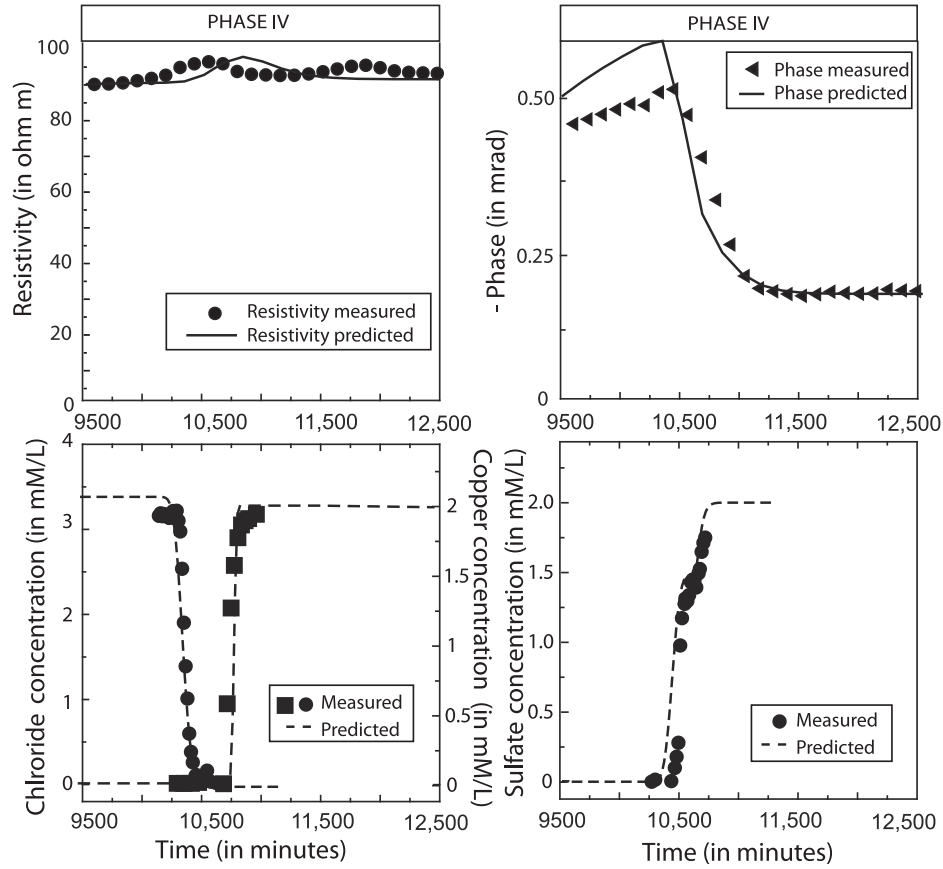
Figure 10. Evolution of the resistivity, phase angle (uncertainty <0.2 mrad), and chloride, sulfate, and copper concentrations during the transition between phase II (flushing of a NaCl solution) and phase III (flushing of a CuSO₄ solution). The dashed lines correspond to the chemical modeling of the concentrations with the reactive transport model with PHREEQC including copper. The solid lines are the results of the modeling of the phase and the resistivity during transport. The resistivity and the phase angle are reported at 183 mHz. Note the delay in the advection of the sulfate, which is also reproduced by the reactive transport model because of retardation.

Appendix A]. The complex conductivity of the solid grain σ_S^* is defined by

$$\sigma_S^* = \sigma_S' + i(\sigma_S'' + \omega \varepsilon_S), \qquad (60)$$

and for frequencies far below the relaxation frequency of water, the complex conductivity of water σ_f^* is given by

$$\sigma_f^* = \sigma_f' + i\omega \varepsilon_f. \qquad (61)$$

[53] In the following, we will use $\varepsilon_f = 80 \pm 1\,\varepsilon_0$ (pure water) and $\varepsilon_s = (4.6 \pm 0.8)\,\varepsilon_0$ (quartz) as representative values for the permittivity of the pore water and the grains, respectively. The constant ε_0 is the permittivity of vacuum (8.854×10^{-12} F m^{-1}). In the following, we use a Cole-Cole distribution of polarization length scales:

$$f(d) = \frac{1}{\pi d} \frac{\sin[\pi(1-\alpha)]}{\cosh[2\alpha \ln(d/d_{50})] - \cos[\pi(1-\alpha)]}, \qquad (62)$$

Table 4. Peak Frequencies of the Polarization Spectra[a]

Species	Ionic Mobility β_i (m² s⁻¹ V)	Diffusion Coefficient D_i[b] (m² s⁻¹)	Relaxation Time τ_0[c] (s)	Peak Frequency[d] (mHz)
Na⁺	5.14×10^{-8}	1.32×10^{-9}	0.95	168
Cl⁻	8.47×10^{-8}	2.18×10^{-9}	-	-
Cu²⁺	5.52×10^{-8}	7.10×10^{-10}	1.76	90
SO₄²⁻	4.14×10^{-8}	5.32×10^{-10}	-	-

[a]The ionic mobilities are from *Revil et al.* [1998, Table 1].
[b]Using $D_i = k_B T \beta_i / |q_i|$, where k_B is Boltzmann's constant (1.3807×10^{-23} J K⁻¹), $T = 298$ K is the absolute temperature, and $|q_i|$ is the absolute value of the charge of the counterions.
[c]Using $\tau_0 = d_0^2/8D_{(+)}$ with $d_0 = 100\ \mu m$.
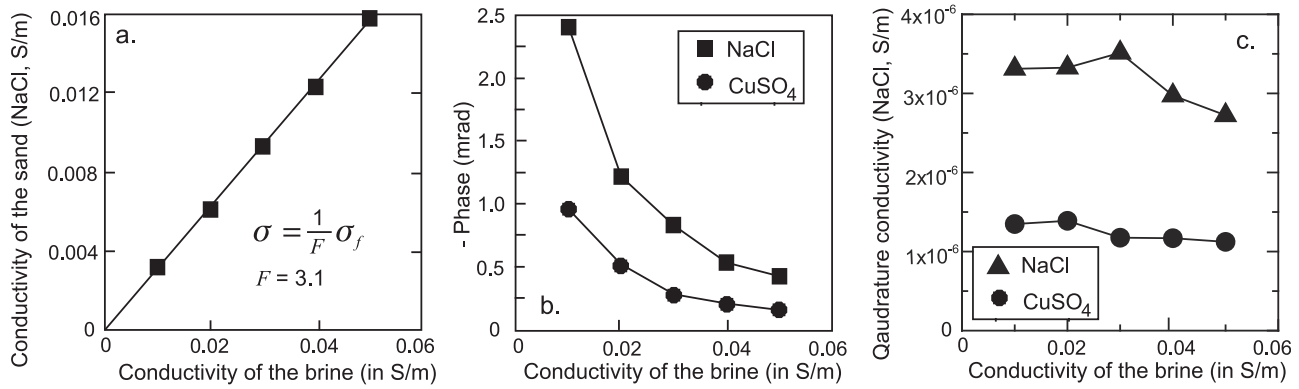[d]Using $f_{peak} \approx 4D_{(+)}/(\pi d_0^2)$.

Figure 11. (a) Conductivity of the sand versus the conductivity of the brine (second set of experiments). The inverse of the slope provides the value of the formation factor. (b) Phase versus the conductivity of the brine (sodium chloride and copper sulfate solutions). (c) Quadrature conductivity versus the conductivity of the brine. The measurements are reported at 183 mHz.

$$\int_{0}^{+\infty} f(d)\mathrm{d}d = 1 \, , \qquad (63)$$

where d_{50} represents the median of the polarization length scale distribution and α is the Cole-Cole exponent ($0 \leq \alpha \leq 1$, where $\alpha = 1$ corresponds to a Debye model). In this case, surface conductivity is described by a Cole-Cole model:

$$\sigma_S = \sigma_S^{\infty} + \frac{\sigma_S^0 - \sigma_S^{\infty}}{1 + (i\omega\tau)^{\alpha}} \, , \qquad (64)$$

$$\sigma_S^0 = \frac{4}{d_0}\Sigma^d \, , \qquad (65)$$

$$\sigma_S^{\infty} = \frac{4}{d_0}\left(\Sigma^d + \Sigma^S\right) . \qquad (66)$$

[54] Such a model accounts for the broad distribution of relaxation times between the relaxation time of the grain and the relaxation time of the Maxwell-Wagner polarization. A comparison between the prediction of such a model

and the experimental data is shown in Figure 13 using $\varepsilon_f = 81\,\varepsilon_0$ and $\varepsilon_S = 5\,\varepsilon_0$. The model reproduces the data quite well over the frequency range investigated (10 mHz to 10 kHz) but requires a distribution of polarization length scales much broader than the grain size distribution.

[55] A second possibility to explain the broad distribution of relaxation times is that there are nonlinear interactions between the dipole moments of each grain, broadening the apparent distribution of polarization length scales (D. Lesmes, personal communication, 2010). A pore-scale model would be needed to check this prediction for a collection of grains immersed in an electrolyte.

[56] A third possibility to explain the broadness of the relaxation time distribution would be to account for membrane polarization. We know that for a given grain size distribution, membrane polarization produces a distribution that is broader than the Stern layer polarization [*de Lima and Sharma*, 1992]. We plan, in a future contribution, to develop a unified model of low-frequency polarization including membrane polarization, Stern layer polarization, Maxwell-Wagner polarization, and the Debye-Falkenhagen effect.

6. Conclusions

[57] Our research was motivated by the need to develop new nonintrusive approaches to characterize contaminant plumes and to bridge the gap between reactive transport code modeling and time lapse−induced polarization measurements. We performed a set of experiments showing the change in complex resistivity associated with the advective transport of a copper sulfate solution in a sand column. These data have been explained with a model connecting the complex conductivity of the porous material to a speciation model for sodium and copper onto the silica surface of the grains. The following conclusions are reached. (1) When surface conductivity can be neglected, the macroscopic conductivity depends only on the conductivity of the pore water and may be insensitive to the presence of small amounts of copper in the pore water. (2) Conversely, the phase lag is very sensitive to the presence of copper because the phase is directly sensitive to the speciation of such a metal onto the mineral surface. (3) Experimental data are reasonably well

Table 5. Characteristics of the Solutions Mixed with the Samples of Sand[a]

Solution	C_f (10^{-3} mol L^{-1})	Conductivity[b] (μS/cm)	pH
NaCl	0.9	100	5.8
NaCl	1.6	210	5.5
NaCl	2.6	320	5.3
NaCl	3.4	420	5.2
NaCl	4.5	550	5.1
CuSO$_4$	0.4	110	4.8
CuSO$_4$	0.9	210	4.6
CuSO$_4$	1.5	320	4.5
CuSO$_4$	2	410	4.4
CuSO$_4$	2.6	510	4.4

[a]These characteristics are also used in the TLM to compute the phase angles.
[b]At 25°C.

Table 6. Summary of the Characteristics of the TLM Obtained for Interfaces Between Silica and Solutions of NaCl and $CuSO_4$, Both With Measured Electrical Conductivities of 220 and 410 μS cm^{-1}

Parameter	Units	NaCl		$CuSO_4$	
		220 μS cm^{-1}	410 μS cm^{-1}	220 μS cm^{-1}	410 μS cm^{-1}
φ_0	V	-0.087	-0.069	-0.065	-0.001
φ_β	V	-0.076	-0.058	0.004	0.001
φ_d	V	-0.050	-0.034	-0.002	0.001
Q_0	C m^{-2}	-0.013	-0.013	-0.003	-0.003
Q_β	C m^{-2}	0.008	0.008	0.003	0.003
Q_s	C m^{-2}	0	0	0	0
$\Gamma^0_{>SiO^--Na^+}$	m^{-2}	4.9×10^{16}	4.80×10^{16}	-	-
$\Gamma^0_{>SiOCu^+}$	m^{-2}	-	-	1.0×10^{17}	1.0×10^{17}
$\Gamma^0_{2>SiO^--Cu^{2+}}$	m^{-2}	-	-	9.9×10^{15}	8.3×10^{15}
χ_d	m	7.62×10^{-9}	5.39×10^{-9}	5.07×10^{-9}	3.59×10^{-9}
Σ^S	S	3.91×10^{-9}	4.77×10^{-9}	4.42×10^{-8}	4.42×10^{-8}
Σ^d	S	4.00×10^{-8}	1.98×10^{-8}	1.76×10^{-8}	2.55×10^{-8}

reproduced by a linear conductivity model in which polarization occurs in the Stern layer. (4) The sorption of cations on the surface of silica can occur either as an immobile inner sphere ligand or a mobile outer sphere ligand. An example of an outer sphere ligand is sodium, which is weakly sorbed on the mineral surface. Sodium keeps its hydration shell and is able to move tangentially along the mineral surface in response to an electrical field. In contrast, copper is predicted to get sorbed quite strongly onto the mineral surface, mainly as an inner sphere (immobile) ligand. This strong sorption is responsible for the decrease of the amplitude of the phase in comparison with the case where the counterion is sodium. This demonstrates how complexation on the mineral surface is directly responsible for a change in the value of the phase lag. This presents an exciting perspective in coupling complex resistivity tomography with reactive transport code modeling to constrain, nonintrusively, chemical reactions in contaminant plumes. With modern 24 bit acquisition cards, one can expect a sensitivity on the phase lag on the order of 0.1 mrad in the field, which is low enough to see the phase lag changes reported in this work in field conditions.

Table 7. Resistivity and Phases Measured and Modeled for Frequencies of 183.1 mHz[a]

Electrolyte	Conductivity (μS/cm)	Resistivity (Ωm)		Phase[b] (mrad)	
		Measured	Modeled	Measured	Modeled
NaCl	110	307	311	-2.40 ± 0.03	-2.30
	200	160	166	-1.22 ± 0.10	-1.17
	320	102	102	-0.84 ± 0.02	-0.80
	420	78	78	-0.54 ± 0.05	-0.53
	550	61	60	-0.44 ± 0.10	-0.42
$CuSO_4$	110	307	308	-0.96 ± 0.16	-0.87
	210	160	157	-0.51 ± 0.10	-0.48
	320	102	103	-0.28 ± 0.07	-0.28
	410	78	81	-0.21 ± 0.01	-0.21
	510	61	65	-0.16 ± 0.06	-0.16

[a]The measurements were done on samples of sand filled with solutions of NaCl and $CuSO_4$. The reported errors on the phases are those given by the impedance meter.
[b]The uncertainties are from the measurement system (SIPLab II).

Appendix A: Generalization to a Distribution of Polarization Length Scales

[58] In this appendix, we provide the generalization of the case discussed in the main text to a distribution of polarization length scales. The idea is to use the convolution product (resulting from the superposition principle applied to linear systems) as discussed by *Lesmes and Morgan* [2001] for the diffuse layer polarization model. This idea was applied to the Stern layer polarization model by *Revil and Florsch* [2010]. These polarization length scales include the grain size distribution and possibly the heterogeneities associated with the roughness of the grains, as experimentally shown by *Leroy et al.* [2008]. The conductivity equation remains the same:

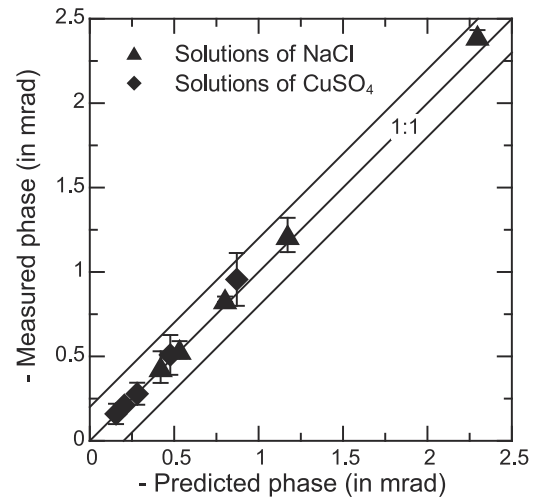$$\sigma(\omega) = \frac{1}{F}[\sigma_w + (F-1)\sigma_S(\omega)], \tag{A1}$$

Figure 12. Comparison between the measured phase and the phase predicted with the model shown in this paper for 10 electrolytes at 183 mHz. The triangles correspond to the solutions of NaCl with conductivities of 100, 210, 320, 420, and 550 μS cm^{-1}, respectively (at 25°C). The diamonds correspond to the solutions of $CuSO_4$ with conductivities of 110, 210, 320, 410, and 510 μS cm^{-1}, respectively.
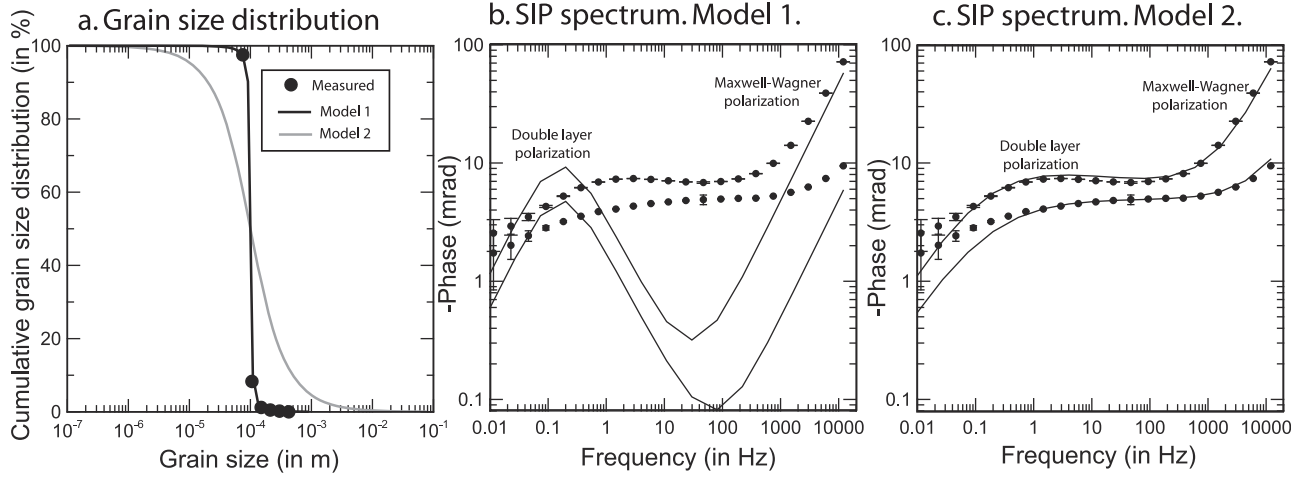
Figure 13. Measured grain size distribution and models used for the convolution in the SIP model. (a) Grain size distribution. The solid circles represent the measured grain size distribution. Model 1, Cole-Cole probability distribution with $d_{50} = 100 \ \mu$m and $a = 0.98$); model 2, Cole-Cole probability distribution with $d_{50} = 100 \ \mu$m and $a = 0.55$. (b) Phase versus frequency and comparison with the model fitting the grain size distribution (model 1). (c) Phase versus frequency and comparison with model 2.

but now the complex surface conductivity is given by

$$\sigma_S(\omega) = 4E_h\Sigma^d + 4E_h\Sigma^S \left(1 - \int\limits_0^\infty \frac{g(\tau)}{1 + i\omega\tau}\mathrm{d}\tau\right), \qquad (A2)$$

$$E_h = \int\limits_0^{+\infty} f(d)\mathrm{d}\ln d\,, \qquad (A3)$$

$$\int\limits_0^\infty g(\tau)\mathrm{d}\tau = 1\,, \qquad (A4)$$

$$\int\limits_0^\infty f(d)\mathrm{d}d = 1\,. \qquad (A5)$$

[59] In equations (A2)−(A5), E_h (in m^{-1}) is the expected value of the inverse of the grain diameter, $f(d)$ is the probability density of the grain diameter distribution, and $g(\tau)$ represents the probability distribution of the relaxation times τ (both probability density distributions are related to each other by *Revil and Florsch* [2010]). We provide an example in the following to illustrate how the probability distribution on the polarization length scales and the probability distribution on the relaxation times are related to each other.

[60] The surface conductivity $\sigma_S(\omega) = \sigma_S'(\omega) + i\sigma_S''(\omega)$ can be decomposed into a real component and a quadrature component as

$$\sigma_S'(\omega) = \sigma_S^0 + \sigma_S^\infty \left(1 - \int\limits_0^\infty \frac{g(\tau)}{1 + \omega^2\tau^2}\mathrm{d}\tau\right), \qquad (A6)$$

$$\sigma_S''(\omega) = \sigma_S^\infty \int\limits_0^\infty \frac{\omega\tau}{1 + \omega^2\tau^2}\mathrm{d}\tau\,, \qquad (A7)$$

$$\sigma_S^0 = 4\Sigma^S E_h\,, \qquad (A8)$$

$$\sigma_S^\infty = 4\Sigma^S E_h\,. \qquad (A9)$$

[61] We can consider, for instance, that the distribution of the polarization length scale is described by a lognormal distribution:

$$f(d) = \frac{1}{\sqrt{2\pi}\hat{\sigma}}\exp\left[-\frac{(\ln d - \mu)^2}{2\hat{\sigma}^2}\right], \qquad (A10)$$

where $\hat{\sigma} = \ln\sigma_g$ and $\mu = \ln d_{50}$ are the standard deviation and the mean of the polarization length natural logarithm, respectively, σ_g is the geometric standard deviation, and d_{50} represents the median of the polarization length scale distribution. If the distribution of the polarization length scales is associated with the particle size distribution, the median d_{50} (in m) is a measure of the average particle diameter size of the granular material. In this case, the expectation of the distribution of the inverse of the grain size (the raw moment of order −1 of the particle size distribution) is given by

$$E_h = \exp\left(\frac{1}{2}\hat{\sigma}^2 - \mu\right) = \frac{1}{d_{50}}\exp\left(\frac{1}{2}\hat{\sigma}^2\right). \qquad (A11)$$

[62] For such a lognormal distribution of polarization length scales, the related distribution of the relaxation times is given by [*Revil and Florsch*, 2010]

$$g(\tau) = \frac{1}{\sqrt{2\pi}(2\hat{\sigma})\tau} \exp\left[-\left(\frac{\ln(\tau/\tau_0)}{\sqrt{2}(2\hat{\sigma})}\right)\right], \qquad (A12)$$

for which the characteristic time τ_0 is associated with the polarization length scale d_{50}.

Appendix B: Microscopic Description of the Stern Layer Polarization

[63] In order to get a better insight as to what the Stern layer polarization is, we introduce here the microscopic equations describing the physics of the transport of the counterions located in the Stern layer (see *Schwarz* [1962], *Schurr* [1964], and *Rosen et al.*, [1993] for additional details). The existence of the Stern layer of weakly sorbed counterions is demonstrated, for example, by molecular dynamic simulations [*Tournassat et al.*, 2009]. An external field, varying with time as $\mathbf{E} = \mathbf{E}_0 \exp(i\omega t)$, is applied to a grain immersed in a background electrolyte. Because the grains do not move under the influence of the electrical field in a porous material, we can consider that the electrophoretic effect (movement of the particles under the effect of an electrical field) can be safely neglected. Electro-osmosis (movement of the pore water due to the viscous drag of the water by the movement of the counterions) is also neglected. The Stern layer is assumed to be infinitesimally thin. We assume that there is no flux of ions from the diffuse layer into or out of the Stern layer. Under these conditions, the conservation of ionic species along the mineral surface in the Stern layer is

$$\frac{\partial \Gamma_i}{\partial t} = -\nabla_S \cdot \mathbf{j}_i, \qquad (B1)$$

where Γ_k is the concentration of species i at the mineral surface (density of counterions i per surface area), ∇_S denotes a surface divergence (with respect to the curvilinear coordinates describing the mineral surface), and $\mathbf{j}_i$ is the flux density of species i along the mineral surface. The electrostatic equations obeyed by the electrical field in the low-frequency limit of the Maxwell equations are

$$\nabla \cdot \mathbf{E} = \frac{\rho}{\varepsilon}, \qquad (B2)$$

$$\nabla \times \mathbf{E} = 0, \qquad (B3)$$

where ρ is the volumetric charge density and ε is the dielectric constant in the Stern layer. This dielectric constant can be derived from the inner capacitance of the double layer (see section 2.4, equation (50)). Equation (B3) implies, in turn, that the electrical field can be derived from an electrostatic potential ψ, which is distinct from the electrostatic potential of the electrical double layer φ. The flux of species i along the mineral surface is given by the Nernst-Planck local equation:

$$\mathbf{j}_i = -\frac{\beta_i \Gamma_i}{|q_i|} \nabla_S \tilde{\mu}_i, \qquad (B4)$$

$$\mathbf{j}_i = -\frac{\beta_i \Gamma_i}{|q_i|} \nabla_S (q_i \psi + k_B T \ln \Gamma_i), \qquad (B5)$$

$$\mathbf{j}_i = -\frac{\beta_i}{|q_i|} (q_i \Gamma_i \nabla_S \psi + k_B T \nabla_S \Gamma_i), \qquad (B6)$$

where $\tilde{\mu}_i$ denotes the electrochemical potential of species i, ∇_S denotes a surface gradient along the mineral surface, β_i is the (Stern layer) ionic mobility of species i, and $q_i = (\pm 1) z_i e$ is the charge of species i (z_i is the unsigned valence). The tangential mobility of the weakly sorbed counterions is confirmed by nuclear magnetic resonance (NMR) spectroscopy. For instance, in the case of sodium on silica, *Carroll et al.* [2002] showed that sodium forms a mobile outer sphere surface complex on the basis of the narrow line width of the NMR spectra, the lack of a chemical shift from aqueous sodium, and negligible quadrupolar couplings. The question is to know whether the mobility of the counterions in the Stern layer is the same as the mobility in the free electrolyte (free from long-range Coulombic interactions). Electrochemists distinguish two types of sorption: weak sorption in the outer Helhmotz plane (outer sphere ligand) and strong sorption in the inner Helmholtz plane (inner sphere ligand), which is closer to the mineral surface than the former. Sodium and alumina are known to be extreme examples of sorption at the surface of silica. While sodium keeps its hydration layer and seems to have the same mobility along the mineral surface as in the free electrolyte [*Revil and Florsch*, 2010], alumina has no mobility whatsoever along the mineral surface [*Revil et al.*, 1999a]. *Zukoski and Saville* [1986a, 1986b] provided several values regarding the mobility of some counterions in the Stern layer.

[64] According to equation (B4), the lateral transport of the counterions in the Stern layer by electromigration is coupled to diffusion. In other words, the flux density is controlled by the gradient of the electrochemical potential $\tilde{\mu}_i$ of species i, which comprises an electrostatic term and a concentration gradient term (an activity gradient term for a non-ideal solution). Combining equations (B1) and (B4) yields

$$\frac{\partial \Gamma_i}{\partial t} = \frac{\beta_i}{|q_i|} \nabla_S \cdot (q_i \Gamma_i \nabla_S \psi + k_B T \nabla_S \Gamma_i). \qquad (B7)$$

[65] Therefore, both the concentration gradient and the imposed electrical field are locally tangential to the mineral surface. Note that the electrical field resulting from the electrical double layer is normal to the mineral surface, and therefore, the two electrical fields are normal to each other [*Revil and Glover*, 1997]. Concentration gradients and the electrical field provide the driving forces for the migration of the counterions along the Stern layer. The first boundary condition results from the continuity of the tangential component of the electrical field at the interface between the Stern layer and the diffuse layer. The second boundary condition results from the fact that the surface of the grain is insulating and therefore impervious to the transport of the counterions. Finally, Gauss's law states [*Rosen et al.*, 1993] that

$$\left(-\varepsilon \frac{\partial \psi}{\partial r}\right)_{r=d/2} = Q_0 + Q_\beta, \qquad (B8)$$

where Q_0 is the surface charge density, Q_β is the charge density of the Stern layer, and r is the radial distance from

the center of the spherical grain of diameter d. Equations (B1)−(B8) can be solved numerically [see *Schwarz*, 1962; *Schurr*, 1964] or numerically [*Rosen et al.*, 1993]. *Rosen et al.* [1993] considered in their model the possible exchange of counterions between the Stern layer and the diffuse layer, while *Schwarz* [1962] considered that the counterions of the entire electrical double layer can only move tangentially along the mineral surface. However, the kinetics of the sorption/desorption of the counterions is a slow process, and we believe that this effect can be neglected at the frequencies typically considered for induced polarization (generally above 1 mHz). If the microscopic set of equations is solved analytically, the expression of the dipole moment can be inserted into a macroscopic conductivity model giving the expression of the complex conductivity model described in section 2.1.

References

Aristodemou, E., and A. Thomas-Betts (2000), DC resistivity and induced polarisation investigations at a waste disposal site and its environments, *J. Appl. Geophys.*, *44*(2-3), 275−302.

Binley, A., B. Shaw, and S. Henry-Poulter (1996), Flow pathways in porous media: Electrical resistance tomography and dye staining image verification, *Meas. Sci. Technol.*, *7*(3), 384−390.

Binley, A., L. D. Slater, M. Fukes, and G. Cassiani (2005), Relationship between spectral induced polarization and hydraulic properties of saturated and unsaturated sandstone, *Water Resour. Res.*, *41*, W12417, doi:10.1029/2005WR004202.

Bordi, F., C. Cametti, A. Rosi, and A. Calcabrini (1993), Frequency domain electrical conductivity measurements of the passive electrical properties of human lymphocytes, *Biochim. Biophys. Acta Biomembr.*, *1153*(1), 77−88.

Cametti, C., F. de Luca, M. A. Macri, B. Maraviglia, G. Zimatore, F. Bordi, R. Misasi, M. Sorice, L. Lenti, and A. Pavan (1995), To what extent are the passive electrical parameters of lymphocyte membranes deduced from impedance spectroscopy altered by surface roughness and microvillosity?, *Colloids Surf. B*, *3*(5), 309−316.

Carroll, S., R. S. Maxwell, W. Bourcer, S. Martin, and S. Hulsey (2002), Evaluation of silica-water surface chemistry using NMR spectroscopy, *Geochim. Cosmochim. Acta*, *66*(6), 913−926.

Chambers, J., M. Loke, R. Ogilvy, and P. Meldrum (2004), Noninvasive monitoring of DNAPL migration through a saturated porous medium using electrical impedance tomography, *J. Contam. Hydrol.*, *68*, 1−22.

de Lima, O. A. L., and M. M. Sharma (1992), A generalized Maxwell-Wagner theory for membrane polarization in shaly sands, *Geophysics*, *57*, 431−440.

Drolon, H., B. Hoyez, F. Druaux, and A. Faure (2003), Multiscale roughness analysis of particles: Application to the classification of detrital sediments, *Math. Geol.*, *35*(7), 805−817.

Dukhin, S. S., and V. N. Shilov (2002), Nonequilibrium electric surface phenomena and extended electrokinetic characterization of particles, in *Interfacial Electrokinetics and Electrophoresis, Surfactant Sci. Ser.*, vol. 106, edited by A. V. Delgado, pp. 55−85, Dekker, New York.

Grimm, R. E., G. R. Olhoeft, K. McKinley, J. Rossabi, and B. Riha (2005), Nonlinear complex resistivity survey for DNAPL at the Savannah River Site A-014 outfall, *J. Environ. Eng. Geophys.*, *10*(4), 351−364.

Hunter, R. J. (1981), *Zeta Potential in Colloid Science: Principles and Applications*, Academic, New York.

Hyslip, J. P., and L. E. Vallejo (1997), Fractal analysis of the roughness and size distribution of granular materials, *Eng. Geol.*, *48*(3,4), 231−244.

Jougnot, D., A. Revil, and P. Leroy (2009), Diffusion of ionic tracers in the Callovo-Oxfordian clay-rock using the Donnan equilibrium model and the electrical formation factor, *Geochim. Cosmochim. Acta*, *73*, 2712−2726.

Jougnot, D., A. Ghorbani, A. Revil, P. Leroy, and P. Cosenza (2010), Spectral induced polarization of partially saturated clay-rocks: A mechanistic approach, *Geophys. J. Int.*, *180*(1), 210−224, doi:10.1111/j.1365-246X.2009.04426.x.

Le Méhauté, A., and G. Crépy (1983), Introduction to transfer and transport in fractal medium, *Solid State Ionics*, *9−10*, 17−30.

Leroy, P., and A. Revil (2009), Spectral induced polarization of clays and clay-rocks, *J. Geophys. Res.*, *114*, B10202, doi:10.1029/2008JB006114.

Leroy, P., A. Revil, S. Altmann, and C. Tournassat (2007), Modeling the composition of the pore water in a clay-rock geological formation (Callovo-Oxfordian, France), *Geochim. Cosmochim. Acta*, *71*(5), 1087−1097, doi:10.1016/j.gca.2006.11.009.

Leroy, P., A. Revil, A. Kemna, P. Cosenza, and A. Gorbani (2008), Spectral induced polarization of water-saturated packs of glass beads, *J. Colloid Interface Sci.*, *321*(1), 103−117.

Lesmes, D. P., and K. M. Frye (2001), Influence of pore fluid chemistry on the complex conductivity and induced polarization responses of Berea sandstone, *J. Geophys. Res.*, *106*(B3), 4079−4090.

Lesmes, D. P., and F. D. Morgan (2001), Dielectric spectroscopy of sedimentary rocks, *J. Geophys. Res.*, *106*(B7) 13,329−13,346.

Lyklema, J. (2002), The role of surface conduction in the development of electrokinetics, in *Interfacial Electrokinetics and Electrophoresis, Surfactant Sci. Ser.*, vol. 106, edited by A.V. Delgado, pp. 87−97, Dekker, New York.

McDonald, J. R. (1987), *Impedance Spectroscopy: Emphasizing Solid Materials and Analysis*, John Wiley, New York.

Morgan, F. D., F. Scira-Scappuzzo, W. Shi, W. Rodi, J. Sogade, Y. Vichabian, and D. Lesmes (1999), Induced polarization imaging of a jet fuel plume, *Environ. Eng. Geophys. Soc.*, *2*, 541−548.

Mukhopadhyay, S., E. L. Sonnenthal, and N. Spycher (2009), Modeling of coupled heat transfer and reactive transport processes in porous media: Application to seepage studies at Yucca Mountain, Nevada, *J. Porous Media*, *12*(8), 725−748.

Olhoeft, G. R. (1985), Low-frequency electrical properties, *Geophysics*, *50*, 2492−2503.

Olhoeft, G. R. (1986), Direct detection of hydrocarbon and organic chemicals with ground-penetrating radar and complex resistivity, in *Proceedings of the NWWA/API Conference on Petroleum, Hydrocarbons and Organic Chemicals in Ground Water—Prevention, Detection, and Restoration*, pp. 284−305 Natl. Water Well Assoc., Dublin, Ohio.

Parkhust, D. L., and C. A. J. Appelo (1999), User's guide to PHREEQC (version 2)—A computer program for speciation, batch-reaction, one dimensional transport, and inverse geochemical calculations, *U.S. Geol. Surv. Water Resour. Invest. Rep.*, *99−4259*, 312 pp.

Phan, T. N. T, N. Louvard, S. A. Bachiri, J. Persello, and A. Foissy (2004), Adsorption of zinc on colloidal silica, triple layer modelization and aggregation data, *Colloids Surf. A*, *244*, 131−140.

Pride, S. (1994), Governing equations for the coupled electromagnetics and acoustics of porous media, *Phys. Rev. B*, *50*(21), 15,678−15,696.

Revil, A. (1999), Ionic diffusivity, electrical conductivity, membrane and thermoelectric potentials in colloids and granular porous media: a unified model, *J. Colloid Interface Sci.*, *212*, 503−522.

Revil, A., and L. M. Cathles (1999), Permeability of shaly sands, *Water Resour. Res.*, *35*(3), 651−662.

Revil, A., and N. Florsch (2010), Determination of permeability from spectral induced polarization in granular media, *Geophys. J. Int.*, *181*, 1480−1498, doi:10.1111/j.1365-246X.2010.04573.x.

Revil, A., and P. W. J. Glover (1997), Theory of ionic surface electrical conduction in porous media, *Phys. Rev. B*, *55*(3), 1757−1773.

Revil, A., L. M. Cathles, S. Losh, and J. A. Nunn (1998), Electrical conductivity in shaly sands with geophysical applications, *J. Geophys. Res.*, *103*(B10), 23,925−23,936.

Revil, A., P. A. Pezard, and P. W. J. Glover (1999a), Streaming potential in porous media: 1. Theory of the zeta potential, *J. Geophys. Res.*, *104*(B9), 20,021−20,031.

Revil, A., H. Schwaeger, L. M. Cathles, and P. Manhardt (1999b), Streaming potential in porous media: 2. Theory and application to geothermal systems, *J. Geophys. Res.*, *104*(B9), 20,033−20,048.

Rosen, L. A., J. C. Baygents, and D. A. Saville (1993), The interpretation of dielectric response measurements on colloidal dispersions using the dynamic Stern layer model, *J. Chem. Phys.*, *98*(5), 4183−4194.

Schindler, P. W., B. Fürst, R. Dick, and P. U. Wolf (1976), Ligand properties of surface silanol groups. I. surface complex formation with Fe^{3+}, Cu^{2+}, Cd^{2+}, and Pb^{2+}, *J. Colloid Interface Sci.*, *55*, 469−475.

Schmutz, M., A. Revil, P. Vaudelet, M. Batzle, P. Femenía Viñao, and D. D. Werkema (2010), Influence of oil saturation upon spectral induced

polarization of oil bearing sands, *Geophys. J. Int.*, *183*, 211–224, doi:10.1111/j.1365-246X.2010.04751.x.

Schurr, J. M. (1964), On the theory of the dielectric dispersion of spherical colloidal particles in electrolyte solution, *J. Phys. Chem.*, *68*, 2407–2413.

Schwarz, G. (1962), A theory of the low-frequency dielectric dispersion of colloidal particles in electrolyte solution, *J. Phys. Chem.*, *66*, 2636–2642.

Sen, P. N., C. Scala, and M. H. Cohen (1981), A self-similar model for sedimentary rocks with application to the dielectric constant of fused glass beads, *Geophysics*, *46*(5), 781–795.

Slater, L., and D. Lesmes (2002a), IP interpretation in environmental investigations, *Geophysics*, *67*(1), 77–88.

Slater, L., and D. Lesmes (2002b), Electrical-hydraulic relationships observed for unconsolidated sediments, *Water Resour. Res.*, *38*(10), 1213, doi:10.1029/2001WR001075.

Sogade, J. A., et al. (2006), Induced polarization detection of contaminant plumes, *Geophysics*, *71*(3), B75–B84.

Subramaniam, K., V. Vithayaveroj, S. Yiacoumi, and C. Tsouris (2003), Copper uptake by silica and iron oxide under high surface coverage conditions: Surface charge and sorption equilibrium modeling, *J. Colloid Interface Sci.*, *268*, 12–22.

Sverjensky, D. A. (2005), Prediction of the speciation of alkaline earths adsorbed on mineral surfaces in salt solutions, *Geochim. Cosmochim. Acta*, *69*, 225–257.

Tarantola, A. (2005), *Inverse Problem Theory: Methods for Model Parameter Estimation*, Soc. for Ind. and Appl. Math., Philadelphia, Pa.

Tournassat, C., Y. Chapron, P. Leroy, M. Bizi, and F. Boulahya (2009), Comparison of molecular dynamics simulations with triple layer and modified Gouy-Chapman models in 0.1 M NaCl-montmorillonite system, *J. Colloid Interface Sci.*, *339*(2), 533–541.

Vanhala, H. (1997), Mapping oil-contaminated sand and till with the spectral induced polarization (SIP) method, *Geophys. Prospect.*, *45*, 303–326.

Vinegar, H. J., and M. H. Waxman (1984), Induced polarization of shaly sands, *Geophysics*, *49*, 1267–1287.

Wang, M., and A. Revil (2010), Electrochemical charge of silica surface at high ionic strength in narrow channels, *J. Colloid Interface Sci.*, *343*, 381–386.

Wong, P. Z. (1987), Fractal surface in porous media, in *Physics and Chemistry of Porous Media*, vol. 2, edited by J. R. Banavar, J. Koplik, and K.W. Winkler, *AIP Conf. Proc.*, *154*, 304–318.

Zhou, Q. Y. (2007), A sensitivity analysis of DC resistivity prospecting on finite, homogeneous blocks and columns, *Geophysics*, *72*(6), F237–F247.

Zukoski, C. F., and D. A. Saville (1986a), The interpretation of electrokinetic measurements using a dynamic model of the Stern layer. I. The dynamic model, *J. Colloid Interface Sci.*, *114*(1), 32–44.

Zukoski, C. F., and D. A. Saville (1986b), The interpretation of electrokinetic measurements using a dynamic model of the Stern layer. II. Comparisons between theory and experiments, *J. Colloid Interface Sci.*, *114*(1), 45–53.

P. Bégassat, ADEME, 20 avenue du Grésillé, BP 90406, F-49004 Angers CEDEX 1, France. (philippe.begassat@ademe.fr)

M. Franceschi, M. Schmutz, and P. Vaudelet, Institut EGID, University of Bordeaux 3, 1 allée F. Daguin, F-33607 Pessac CEDEX, France. (franceschi@egid.u-bordeaux3.fr; schmutz.myriam@gmail.com; pierre.vaudelet@gmail.com)

A. Revil, Department of Geophysics, Colorado School of Mines, 1500 Illinois St., Golden, CO 80401, USA. (arevil@mines.edu)